Mathematical Modeling of CD8 T Cell Responses to Metabolic Therapy in Cancer

Wesal Hammo, Mo Chen
Mentor: Quiyana Murphy

July 17, 2026

Abstract

Glycolysis, the metabolic pathway by which glucose is broken down to release energy, is profoundly upregulated in many cancers, with tumor cells adopting aerobic glycolysis (the Warburg effect) to sustain rapid proliferation while generating a nutrient-deprived, immunosuppressive microenvironment. This heightened glycolytic demand restricts the metabolic capacity of cytotoxic $CD8^+$ T cells, driving functional exhaustion and enabling tumor progression. Recent work suggests that activating pyruvate kinase M2 (PKM2) can restore T-cell metabolic fitness, enhance effector function, and promote durable immune memory, positioning PKM2 as a promising target for metabolic immunotherapy. Motivated by these findings, we develop a mathematical framework to investigate the impact of PKM2 activation in metastatic melanoma based on published data from a syngeneic, highly metastatic murine melanoma study. Using published B16-F10 melanoma growth data in immunocompromised mice, we identify the von Bertalanffy model as the most biologically realistic tumor growth law. We then construct a system of ordinary differential equations describing tumor dynamics, $CD8^+$ T-cell responses, interferon-γ (IFN-γ)–mediated immune interactions and the pharmacological activation of PKM2. We then analytically examine the-long term behavior of this tumor-immune model, showing that the tumor free equilibrium is unconditionally unstable, deriving an explicit condition under which uncontrolled tumor growth is stable, and reducing the coexistence equilibria to the real positive roots of a single polynomial equation. The model was then extended to incorporate $CD8^+$ T cell memory subsets. To capture the mechanistic origin of PKM2's effects, we further develop a multi-scale extension that couples this population-level framework to an intracellular submodel of glucose uptake, PKM2 conformational dynamics, and ATP production within individual effector T cells, linked to glucose competition and lactate-mediated immunosuppression in the tumor microenvironment. This framework provides a tool for exploring how metabolic interventions may enhance immediate tumor control while supporting long-term anti-tumor immunity.

1 Introduction

Cancer can be defined as the uncontrolled cell growth and acquisition of metastatic properties [1]. Tumor cells differ from normal cells in their lack of response to control mechanisms, allowing continued growth and progression. Although traditional treatment modalities such as surgery, chemotherapy, and radiation therapy remain important components of cancer treatment [2, 3, 4], recent advances in immunotherapy have transformed cancer care by enhancing the immune system's ability to recognize and eliminate malignant cells [5].

In addition to genetic and epigenetic alterations, cancer progression is strongly influenced by metabolic reprogramming. In the 1920s, Otto Warburg published experimental data demonstrating enhanced conversion of glucose to pyruvate even in the presence of abundant oxygen. Warburg hypothesized that defective mitochondrial respiration forces cancer cells to rely on aerobic glycolysis for energy production, a phenomenon now known as the Warburg effect [6]. This metabolic shift has become one of the most recognized hallmarks of cancer and has motivated investigations into metabolic pathways as potential therapeutic targets.

Recent work has highlighted the importance of metabolic regulation in $CD8^+$ T-cell function. Activation of pyruvate kinase M2 (PKM2) through the small molecule agonist TEPP46 resulted in a significant increase in the infiltration and expansion of tumor-infiltrating $CD8^+$ T-cells and enhanced their effector functions

through increased IFN-γ and granzyme B production [7]. PKM2 activation also reduced the expression of exhaustion markers, including PD-1 and LAG-3, improved tumor-cell killing by activated CD8$^+$ T cells, promoted the formation of long-lived memory-like T-cell populations, and significantly slowed tumor growth in B16-F10 melanoma models [7]. These findings suggest that metabolic modulation of T-cell responses may provide a promising strategy for improving anti-tumor immunity.

Despite experimental evidence, the quantitative relationship between PKM2-driven metabolic reprogramming and the cell-to-cell level dynamics of tumor-immune competition remains understudied. Prior ordinary differential equation models of tumor-immune dynamics have characterized the qualitative long-term behavior of tumor growth under immune surveillance, including conditions for tumor elimination, immune escape, and bistability between these outcomes [8, 9]; related frameworks incorporating cytokine-mediated immune signaling have further shown how indirect, cytokine-driven tumor control can be captured within this modeling framework [10]. However, none of these frameworks account for the metabolic state of effector T cells, despite growing evidence that metabolic fitness is a primary determinant of anti-tumor immune function.

In this work, we develop a chain of mathematical models to investigate how PKM2 activation shapes the tumor-immune response in metastatic melanoma. We first fit published B16-F10 melanoma tumor growth data in immunocompromised mice to various tumor growth models to identify a biologically appropriate tumor growth law. Building on this, we construct a system of ordinary differential equations coupling tumor cells, effector CD8$^+$ T cells, and IFN-γ-mediated signaling, with PKM2 activation entering as a treatment-dependent enhancement of immune function. We analytically characterize the long-term behavior of this base model, deriving conditions under which tumor elimination, uncontrolled tumor growth, and stable tumor-immune coexistence occur. We then extend the model to incorporate CD8$^+$ T-cell memory subsets, and further develop a multi-scale formulation linking intracellular PKM2 and glucose metabolism to population-level tumor-immune dynamics. Together, these models provide a quantitative framework for understanding how metabolic interventions such as PKM2 activation may improve immunotherapy outcomes.

2 Materials and Methods

2.1 Data Fitting and Parameter Estimation for Tumor Growth Dynamics

To identify the optimal tumor growth equation for simulating metastatic melanoma, we modeled and fitted the growth kinetics of B16-F10 tumors in immunodeficient mice. Growth data were extracted from six independent published studies. We then evaluated and cross-compared six popular tumor growth dynamics models: Exponential, Logistic, Gompertz I, Gompertz II, Von Bertalanffy I, and Von Bertalanffy II. The Exponential model assumes an idealized environment with unlimited resources, where growth is driven solely by a constant intrinsic rate (r). In contrast, the Logistic model introduces resource limitations, where growth decreases linearly as the population approaches a maximum environmental carrying capacity (K). The Gompertz 1 and Gompertz 2 models account for factors like tumor aging and necrotic core development by incorporating an exponentially decaying growth rate, which diminishes either as a function of time (governed by initial growth rate G_0 and decay constant α) or as a function of tumor volume (governed by decay factor a and inverse capacity b). Finally, the Von Bertalanffy 1 and Von Bertalanffy 2 models apply metabolic scaling laws to treat the tumor as a three-dimensional structure, asserting that nutrient-driven proliferation scales with the tumor's surface area (anabolic parameter α) while cellular decay scale with its overall volume (catabolic parameter β).

For data processing, the initial time and tumor size for each dataset were extracted and fixed according to the original papers. A summary of the tumor growth models can be found in Table 1.

2.1.1 Methodology and Parameter Estimation

In the parameter estimation phase, we utilized both Mathematica and MATLAB. First, Mathematica scripts were written to generate initial parameter guesses for each model. To describe how well the models predict tumor growth while mitigating the influence of extreme values, we constructed a log-scaled sum of squared

errors (SSE) distance function. By calling the `fminsearch` function in MATLAB (based on the Nelder–Mead simplex algorithm), non-linear optimization was performed to find the optimal parameter set $\hat{\theta}$ that minimizes the distance function, formulated as:

$$\hat{\theta} = \arg\min_{\theta} \sum_{j=1}^{n} \left[\log(T_{\text{model}}(t_j;\theta)) - \log(T_{\text{data}}(t_j))\right]^2 \tag{1}$$

where t_j represents the measurement time, T_{model} is the model-predicted tumor volume, T_{data} is the experimental observation, n is the total number of data points, and θ is the parameter vector for each model as listed in Table 1.

2.1.2 Model Selection Criteria

To determine which model is the best with the current parameters, we calculate their Akaike information criterion (AIC) values [11]. Given the relatively small size of our datasets, we adopted the corrected Akaike Information Criterion (AICc) as the core metric for model selection to balance goodness of fit against model complexity (thereby preventing overfitting). AICc evaluates the fit quality while penalizing the number of fitted parameters k. Under this framework, the model with the minimum AICc value (min-AICc) is considered the best-fit model. Furthermore, when the difference between a model's AICc value and minimum AICc value is less than or equal to 4 ($\text{AICc}_i - AICc_{min} \leq 4$), the models are deemed to have equivalent performance for that dataset.

Model	**Equation**	Number of parameters (k)	Parameter vector (θ)
Exponential	$\frac{dT}{dt} = rT$	1	r
Logistic	$\frac{dT}{dt} = rT\left(1 - \frac{T}{K}\right)$	2	r,K
Gompertz I	$\frac{dT}{dt} = G_0 e^{-\alpha t} T$	2	G_0, α
Gompertz II	$\frac{dT}{dt} = aT\ln(\frac{1}{bT})$	2	a,b
Von Bertalanffy I	$\frac{dT}{dt} = \alpha T^{2/3} - \beta T$	2	α, β
Von Bertalanffy II	$\frac{dT}{dt} = \alpha T\left((\beta T)^{2/3} - 1\right)$	2	α, β

Table 1: Overview of tumor growth models: equations, analytical solutions, and parameter counts. T is the number of tumor cells, t is time in hours, T_0 is the initial number of tumor cells at time of control experiments.

2.1.3 Description of Datasets for fitting

Dataset 1

The tumor growth data used in this analysis were obtained from the paper "Antitumor effect of pharmacologic ascorbate in the B16 murine melanoma model" [12]. Specifically, daily tumor volume data were digitally extracted from the N.S. (non-obese diabetic severe combined immunodeficiency) control group in Figure 10 (see Appendix 7.1) using WebPlotDigitizer [13]. These mice lack mature B, T, and NK cells. In the in

vivo experiment, tumors were induced by subcutaneously injecting 1×10^5 B16-F10 melanoma cells into the shaved lateral right flank of 8- to 12-week-old male NOD-scid mice, with a sample size of 12. For the purpose of this analysis, the number of tumor cells per cubic millimeter is set to be 1×10^6. Five days after the injection of tumor cells, the mice were treated by intraperitoneal (ip) injection twice daily with 3 g/kg normal saline. Tracked via electronic digital calipers, the tumors grew to a maximum volume of approximately $1300mm^3$ before the mice were sacrificed 14 days post-injection. Mice's weights were not tracked in this group of experiment. Finally, to fit the tumor growth models to this dataset, an initial guess was produced by an estimation done with Mathematica.

Dataset 2

The tumor growth data used in this analysis were obtained from the study "Synergy between Toxoplasma gondii type I GRA17 immunotherapy and PD-L1 checkpoint inhibition triggers the regression of targeted and distal tumors," [14] which investigated the growth and treatment response of B16-F10 melanoma tumors in a murine model. The experiment utilized five female NOD/SCID/IL-2gR knockout mice aged 6–8 weeks. These mice lack T cells, B cells, and Natural Killer cells, and have defective macrophages. To establish the tumors, 1×10^6 to 3×10^6 B16-F10 melanoma cells were injected subcutaneously into the right flank of each mouse. The data used for model fitting correspond to the control group treated with phosphate-buffered saline (PBS) following tumor implantation. Survival and body weight were monitored throughout the study, and mice were euthanized upon reaching humane endpoints, including a body weight loss of 20%, a body condition score of 2 or less, or a tumor diameter of approximately 1.5 cm. Tumor volume was measured using digital calipers beginning on day 9 after implantation and every other day thereafter until day 19. For this analysis, tumor growth data were digitally extracted from the corresponding figure in the publication using the MATLAB Grabit tool [13] from Figure 11 (see Appendix 7.1).

Dataset 3

This dataset comes from the paper "External Magnet Improves Antitumor Effect of Vinblastine and the Suppression of Metastasis" [15]. The experiments were conducted using female SCID mice (which lack functional T and B lymphocytes) aged 10–12 weeks. Each mouse was injected with (1×10^6) B16-F10 melanoma cells, although the precise injection site was not specified. Treatment began on day 12, when tumor volumes reached approximately 100 mm^3. Tumor size was measured daily using digital calipers, and tumor volume was calculated from these measurements. The study concluded around day 16, when untreated tumors reached approximately 700 mm^3. In some mice, a thick callous layer developed over the tumors within five days of treatment initiation, necessitating early termination of the experiment. The data analyzed here represent the saline-treated control group as shown in Figure 12 (see Appendix 7.1).

Dataset 4

This analysis utilizes data from the study "Rose Bengal–Amphiphilic Peptide Conjugate for Enhanced Photodynamic Therapy of Malignant Melanoma" [16]. The experiments were conducted using SCID mice, which lack functional T and B lymphocytes; however, the sex and age of the animals were not specified. Each mouse was injected with 3×10^5 B16-F10 melanoma cells in the rear dorsum. Treatment began four days after tumor cell inoculation, when tumors had reached an average volume of 80 mm^3. Tumor volume was monitored throughout the 12-day treatment period, and the animals were euthanized on day 13. The authors reported that untreated tumors were 573% larger than their pretreatment volume 12 days after treatment initiation. The data analyzed in this report represent the untreated control group as shown in Figure 13 (see Appendix 7.1).

Dataset 5

In vivo tumor growth data was digitally extracted from online supplemental Figure 14 (see Appendix 7.1) of the paper "Self-assembly nanovaccine containing TLR7/8 agonist and STAT3 inhibitor enhances tumor immunotherapy by augmenting tumor-specific immune response" [17], using the WebPlotDigitizer tool [13]. The study evaluated the growth of B16/F10-OVA melanoma in 6-week-old male NOD SCID (non-obese diabetic severe combined immunodeficiency) mice. The tumors were developed by subcutaneously injecting the melanoma cells, and the sample size was not explicitly mentioned, but the parallel group consisted of 5 mice per group. Tumor volumes were calculated iteratively over the study period, with the assumption that 1 cubic millimeter equates to 1×10^6 tumor cells. The mice were monitored until the maximum tumor volume reached approximately 2200 mm^3 at day 22 post-injection. Body weights was not tracked. Survival data was not explicitly given. Based on the Akaike Information Criterion (AICc), the Von Bertalanffy 1

model provided the best fit for the data, yielding the lowest AICc value of -26.69 and an SSE of 0.1278.

Dataset 6

The tumor growth data used in this analysis were obtained from Figure 15 (see Appendix 7.1) of paper "Inhibition of Vps34 reprograms cold into hot inflamed tumors and improves anti–PD-1/PD-L1 immunotherapy" [18]. This study evaluates the in vivo growth dynamics of B16-F10 tumors, comparing control (shCT) and Vps34-knockdown (shVps34) groups within an immunodeficient NSG mouse model. NSG stands for NOD scid gamma mice, which is a specific type of NOD SCID mice mentioned above. Mice were injected subcutaneously in the right flank with B16-F10 cell lines diluted in 100 μl of phosphate-buffered saline. The sex of the mice is not specifically mentioned. Tumor progression was monitored through longitudinal growth curves, and final tumor weights were quantitatively assessed in grams at day 17 post-inoculation. The sample sizes for these experiments consisted of 10 mice per group for the primary growth and weight analyses. We assume that 1 cubic millimeter equates to 1×10^6 tumor cells.

A summary of experimental datasets can be found in Table 14.

2.2 Mathematical Modeling

2.3 Model 1

Mathematical models provide a useful framework for studying the complex interactions between tumor cells and the immune system while evaluating potential therapeutic strategies. In this work, we develop a system of ordinary differential equations to describe the dynamics of tumor cells, effector $CD8^+$ T cells, interferon-γ (IFN-γ), and PKM2 activation in the presence of TEPP46 treatment. The model captures the effects of tumor growth, immune-mediated tumor killing, cytokine production, and PKM2-induced enhancement of $CD8^+$ T-cell function. This initial framework serves as the foundation for a more biologically detailed model that incorporates distinct effector and memory $CD8^+$ T-cell subsets.

Equations

Variable	Description	Units
T	Tumor cell population	Total number of tumor cells
E	Antigen-positive effector CD8+ T Cells	Total number of CD8+T cells
F	IFN-γ concentration	pg/ml
P	PKM2 activity induced by TEPP46 treatment	

Table 2: State variables of Model 1 given in Equations (2)-(4)

.

$$\frac{dT}{dt} = (\alpha T^{2/3} - \beta T) - \delta_E \frac{(E/T)^\lambda}{s + (E/T)^\lambda} T(1 + \gamma_1 P) - \delta_F \frac{T}{h_{T,F} + T} F \tag{2}$$

Equation (2) follows the growth and decay of the tumor cell population. The tumor growth follows a von Bertalanffy (VB) law represented by the term $\alpha T^{2/3} - \beta T$ which captures a sublinear growth through (α) and the observation that tumor expansion slows down as size increases (β) and it was selected after some computation data fitting experiments. The decay of the tumor happens through two mechanisms of immune mediated killing. The first one is effector CD8 T cells killing the tumor cells via the term $\delta_E \frac{(E/T)^\lambda}{s+(E/T)^\lambda}$, which was adapted from de Pillis and Radunskaya [8]. In this expression (δ_E) is the maximum effector-cell-mediated tumor killing rate, (E/T) is the effector to tumor cell ratio, (s) is the saturation constant controlling the magnitude of the killing response, and (λ) is the dimensionless Hill coefficient that controls the steepness of the killing response as E/T increases. This saturating form reflects the limited cytotoxic capacity of effector cells at high tumor volume. Our effector-mediated killing term is also being multiplied by the factor $(1+\gamma_1 P)$, which phenomenologically represents the enhancement of $CD8^+$ T-cell cytotoxic function induced by PKM2 activation. Cytokine-mediated killing by IFN $-\gamma$ is represented by the term $\delta_F \frac{T}{h_{T,F}+T} F$, consistent with

prior models [10] in which cytokine signaling within the IFN $-\gamma$ pathway is modeled with saturation. Here, (δ_F) is the maximum IFN $-\gamma$-mediated tumor killing rate, (F) is the concentration of IFN $-\gamma$, and $(h_{T,F})$ is the half-saturation constant.

$$\frac{dE}{dt} = \frac{T}{h_{E,T}+T}E(p_E + \sigma_F F) - \frac{c_T T E}{1+\gamma_3 P} - \mu_E E \tag{3}$$

Equation (3) models the effector CD8 T-cell population. Since CD8 T-cells are antigen-specific immune responders, their growth is driven by tumor antigen stimulation represented by $(\frac{T}{h_{E,T}+T}E(p_E + \sigma_F F))$. This Michaelis-Menten form captures the saturation of antigen-dependent activation at high tumor burdens, seen previously in Yu et al. [10]. Here, (p_E) is the baseline proliferation rate of effector CD8$^+$ T-cells, while (σ_F) quantifies the enhancement of effector cell proliferation by IFN $-\gamma$, and $(h_{E,T})$ denotes the half saturation constant describing the tumor burden at which antigen-driven proliferation reaches one-half its maximum capacity. Effector CD8$^+$ T-cells undergo decay through two mechanisms. The first is exhaustion and inactivation after repeated encounters with tumor cells represented by the term $(\frac{c_T T E}{1+\gamma_3 P})$. In this expression c_T is the tumor-induced exhaustion rate, while the factor $(1+\gamma_3 P)$ phenomenologically captures the protective effect of PKM2 against T-cell dysfunction [7]. The second mechanism is natural effector-cell death represented by the term $(\mu_E E)$.

$$\frac{dF}{dt} = p_F \frac{T}{h_{F,T}+T}E(1+\gamma_2 P) - \mu_F F \tag{4}$$

Equation (4) describes the concentration of IFN $-\gamma$ which is a key cytokine produced by active effector cells. IFN$-\gamma$ production is driven by antigen-stimulated effector cells, modeled by the term $(p_F \frac{T}{h_{F,T}+T}E(1+\gamma_2 P))$. In $(p_F \frac{T}{h_{F,T}+T}E)$ the saturation dependence on tumor burden reflects the fact that cytokine secretion is limited by the finite capacity of the cellular machinery responsible for producing IFN $-\gamma$, the term was adapted from Yu et al. [10]. PKM2 activation enhances cytokine output through $(1+\gamma_2 P)$ [7]. IFN $-\gamma$ decays at a natural rate via $(\mu_F F)$.

While most models choose not to model it, IFN-γ is included as an independent state variable in our framework because PKM2 activation has been reported to enhance IFN-γ production by activated CD8$^+$ T cells, and IFN-γ contributes to indirect tumor control in addition to direct cytotoxicity.

All together the Tumor-Immune System with PKM2 treatment can be written as **Model 1:**

$$\frac{dT}{dt} = (\alpha T^{2/3} - \beta T) - \delta_E \frac{(E/T)^\lambda}{s+(E/T)^\lambda}T(1+\gamma_1 P) - \delta_F \frac{T}{h_{T,F}+T}F, \tag{5a}$$

$$\frac{dE}{dt} = \frac{T}{h_{E,T}+T}E(p_E + \sigma_F F) - \frac{c_T T E}{1+\gamma_3 P} - \mu_E E,, \tag{5b}$$

$$\frac{dF}{dt} = p_F \frac{T}{h_{F,T}+T}E(1+\gamma_2 P) - \mu_F F. \tag{5c}$$

The corresponding parameters to Model 1 presented in System (5) are given in Table 3.

2.4 Model Diagram

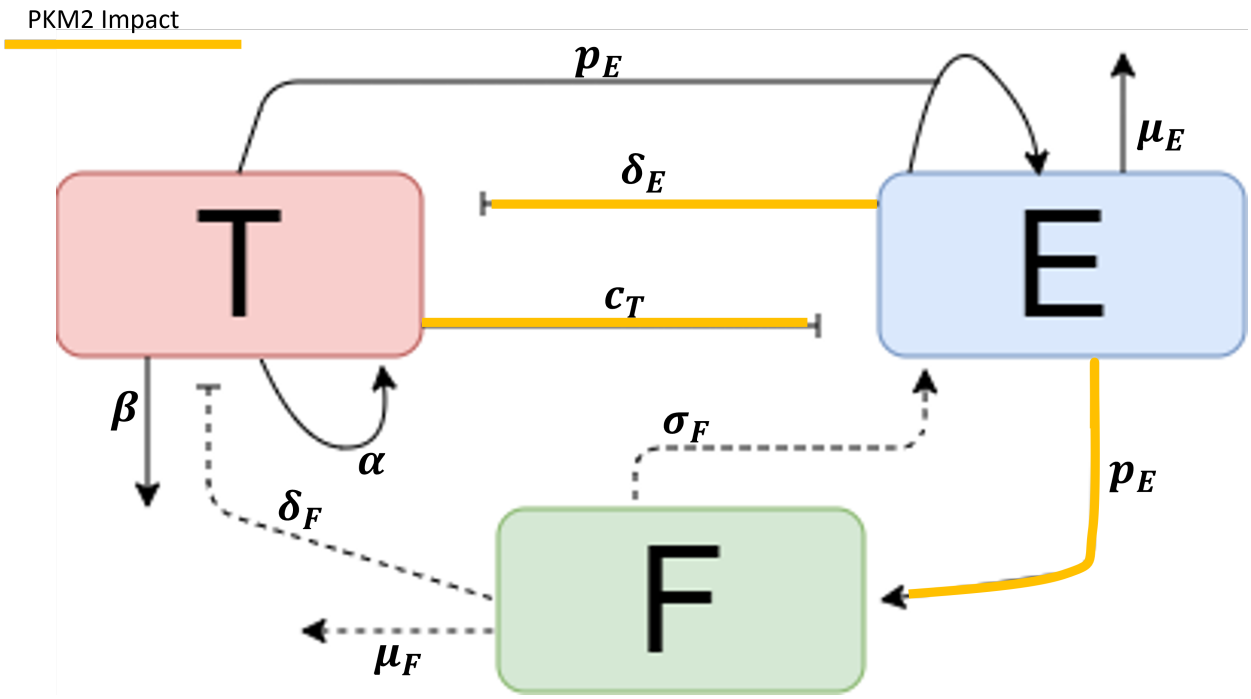


Figure 1: Interaction network of the tumor (T), effector $CD8^+$ T-cels (E), and IFN-γ (F) populations for Model 1 given in System (5). Solid arrows denote proliferation, activation and production processes; dashed arrows denote cytokine mediated effects, and blunt ended arrows denote killing and inhibition.

Parameter	Description	Units
Tumor Dynamics		
α	Tumor growth rate constant (von Bertalanffy sublinear growth)	Number of tumor cells$^{1/3} \cdot \mathrm{h}^{-1}$
β	Tumor death rate constant (von Bertalanffy decay)	h^{-1}
δ_E	Maximum Effector-mediated tumor killing rate	h^{-1}
s	Tumor half-saturation constant in immune killing term	Dimensionless
λ	Hill coefficient for immune killing saturation	Dimensionless
δ_F	Maximum IFN-γ mediated tumor killing rate	Number of tumor cells $(\mathrm{pg/ml})^{-1}\mathrm{h}^{-1}$
γ_1	PKM2 enhancement of effector-mediated tumor killing	$\mathrm{pg/ml}^{-1}$
Effector CD8 T cells (E)		
p_E	Baseline antigen-driven effector cell proliferation rate	h^{-1}
σ_F	Strength of IFN-γ enhancement of effector proliferation	$(\mathrm{pg/ml})^{-1}\mathrm{h}^{-1}$
$h_{E,T}$	Tumor half-saturation constant for effector stimulation	Number of Tumor cells
c_T	Tumor-induced effector cell exhaustion rate	Number of tumor cells $^{-1}\mathrm{h}^{-1}$
μ_E	Natural effector cell death rate	h^{-1}
p_F	IFN-γ production rate by activated effector cells	pg/ml Number of CD8T cells $^{-1}\mathrm{h}^{-1}$
$h_{F,T}$	Tumor half-saturation constant for IFN-γ production	Number of tumor cells
γ_2	PKM2 enhancement of IFN-γ production	$\mathrm{pg/ml}^{-1}$
μ_F	IFN-γ decay rate	h^{-1}

Table 3: Model parameters, descriptions, and dimensional units for Model 1 (Tumor-Immune Model) with PKM2 treatment presented in System (2)-(4).

2.5 Model 2

The initial model described interactions between tumor cells, effector CD8$^+$ T cells, interferon-γ (IFN-γ), and PKM2 activation to investigate the effects of TEPP46 on anti-tumor immunity. While this framework captured the overall immune response, it treated the effector CD8$^+$ T-cell population as a single homogeneous compartment. Experimental studies have shown that activated CD8$^+$ T cells differentiate into functionally distinct subsets [19] with different proliferative capacities, cytotoxic functions, and long-term memory potential. To better represent these biological processes, the model is extended by subdividing the effector population into effector cells (ECs), short-lived effector cells (SLECs), and memory precursor effector cells (MPECs) [20]. This extension enables the model to capture effector differentiation, memory formation, and antigen-driven memory reactivation while incorporating the proposed effects of PKM2 activation on CD8$^+$ T-cell fate decisions.

Variable	Description	Units
T	Tumor cell population	Total number of tumor cells
E	Effector CD8 T-Cells (ECs)	Total number of effector CD8 T cells
S	Short-Lived Effector CD8 T-Cells (SLECs)	Number of S cells
M	Memory Precursor Effector CD8 T-Cells (MPECs)	Number of M cells
F	IFN-γ concentration	pg/ml

Table 4: State variables of Model 2 given in Equations (6)-(10).

While there exist lots of different memory differentiation pathways proposed in literature depending on the antigen and type of immune cells being studied, our framework closely followed the one experimentally

validated by Crauste et al. [20] using the same memory cell markers and phenotype from Farsani et al. [7]. Cell states were defined by CD44, KLRG1^{+}CD127^{-} and KLRG1^{-}CD127^{+} corresponding to short-lived effector cell (SLEC) and memory precursor effector cells (MPEC) populations respectively. Using a pathway that matches our available data allows us to incorporate these cell populations in our model in a biologically consistent way. The pathway goes according to Figure 2.

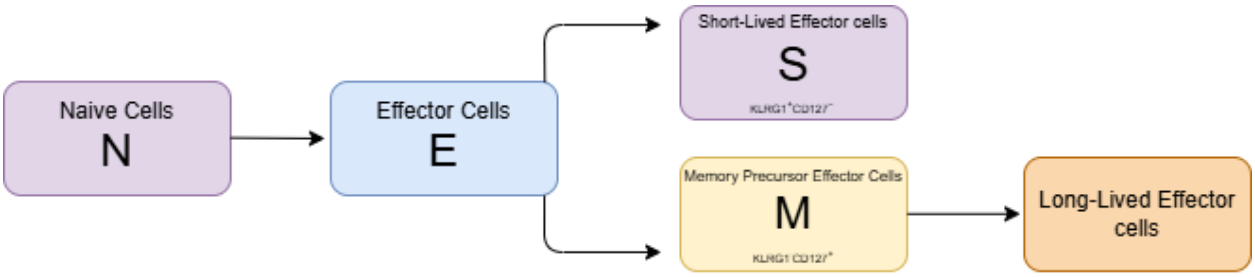


Figure 2: CD8 T-cell memory differentiation pathway based on Crauste et al. [20]

While this paper is built on immune response against virus infection, we assume the mechanism works similarly for tumor.
Additionally, model assumes that the Effector Cells and short-lived effector cells are both capable of killing tumor cells and are both capable of secreting $IFN-\gamma$.

Tumor Dynamics:

$$\frac{dT}{dt} = (\alpha T^{2/3} - \beta T) - \delta_E \frac{(\frac{E}{T})^{\lambda}}{s + (\frac{E}{T})^{\lambda}} T(1 + \gamma_1 P) - \delta_F \frac{T}{h_{T,F} + T} F - \delta_S \frac{T}{h_{T,S} + T} S \tag{6}$$

Equation (6) models tumor growth and immune mediated killing. The tumor cells grow according to a von Bertalanffy law $\alpha T^{2/3} - \beta T$ which reflects a sublinear growth at large tumor sizes. This model assumes that effector cells and short-lived effector cells (SLECs) kill tumor cells represented by $\delta_E \frac{(\frac{E}{T})^{\lambda}}{s+(\frac{E}{T})^{\lambda}} T$ a formulation adapted from de Pillis and Radunskaya [8] and we assume a similar mechanism for the short effector cells with $\delta_S \frac{T}{h_{T,S}+T} S$. The two saturating interaction terms capture the limited cytotoxic capacity of effector cells. Similar to the implementation in model 1, PKM2 activation further enhances immune killing by the effector cells (E) through the factor $(1 + \gamma_1 P)$. Furthermore, IFN $-\gamma$ contributes additional tumor killing through $\delta_F \frac{T}{h_{T,F}+T}$ [10].

Naive Cells (N):

Although the memory differentiation pathway study that this model closely follows [20] includes a naive CD8 T cell compartment, we do not explicitly track the naive CD8 T cell population. Since PKM2 activation primarily affects antigen-experienced CD8 T cells [7] by enhancing their mitochondrial function and effector activity, and naive cells act as an initial baseline population with very limited direct involvement with tumor control, we opt out of modeling naive CD8 T cells and instead start our differentiation pathway at the effector stage.

Effector CD8 T-Cells (E):

$$\frac{dE}{dt} = \frac{pT}{h_{E,T} + T} E - \mu_E E^2 - d_{E,S} E(1 - \gamma_1 P) - d_{E,M} E(1 + \gamma_2 P) + \frac{p_M T}{h_{M,T} + T} M - \frac{c_T T E}{1 + \gamma_3 P} \tag{7}$$

Equation (7) models the effector CD8 T cell population. Because the model begins after the initial antigen priming, effector cells expand in response to tumor burden through the antigen-dependent proliferation term $\frac{pT}{h_{E,T}+T} E$, a Michaelis-Menten form that captures the saturating nature of antigen-driven activation. Density-dependent death is modeled by $\mu_E E^2$, adapted from Crauste et al. [20] and accounts for the limited proliferative capacity of effector cells and the increased likelihood of apoptosis as the effector population becomes crowded. Effector cells go through additional decay in the form of exhaustion and inactivation following repeated encounters with tumor cells/antigens, and that is represented by the term $c_T TE$, and

this exhaustion has been shown to be reduced by PKM2 through down regulation of exhaustion markers PD1 and LAG3 [21] which is modeled through the factor $(1+\gamma_3 P)$. Effector cells differentiate into short-lived effector cells (SLECs) or memory precursor effector cells (MPECs) at rates $d_{E,S}$ and $d_{E,M}$ respectively. PKM2 activation modulates these fate decisions such that the factor $(1-\gamma_1 P)$ reduces the differentiation into SLECs while $(1+\gamma_1 P)$ enhances differentiation into MPECs. These additions to the model are consistent with experimental findings that PKM2 activation promotes the development of long-lived effector subsets instead of terminally differentiated SLECs [7]. Memory-precursor and stem-like CD8 T cell subsets have been shown to re-enter the effector pool upon antigen re-encounter, differentiating into new effector populations that sustain long-term tumor control [19]. This addition is represented through the term $\frac{p_M T}{h_{M,T}+T} M$ [22].

Short-Lived Effector Cells (S):

$$\frac{dS}{dt} = d_{E,S} E(1-\gamma_1 P) + \rho_S T S - \mu_S S^2 - \mu_S S \tag{8}$$

Equation (8) describes the SLEC (KLRG1$^+$CD127$^-$ markers) population, a highly cytotoxic subset of CD8$^+$ T-cells responsible for direct tumor killing. SLECs arise from ECs at rate $(d_{E,S})$, while the factor $(1-\gamma_1 P)$ captures the reduction in SLEC differentiation induced by PKM2 activation [7]. Tumor antigen stimulates further expansion through $\rho_S T S$, where ρ_S is the tumor-stimulated proliferation rate. SLECs are lost through both density-dependent death, modeled via $\mu_S S^2$, and natural turnover, represented through the linear death term $\mu_S S$. These decay terms reflect the limited lifespan and terminally differentiated nature of the SLEC population, as previously seen in Crauste et al. [20].

Memory Cells (M):

$$\frac{dM}{dt} = d_{E,M} E(1+\gamma_2 P) - \mu_M M - \frac{p_M T}{h_{M,T}+T} M \tag{9}$$

Equation (9) models the memory precursor population (KLRG1$^-$CD127$^+$ markers). MPECs arise from the ECs at rate $d_{E,M} E(1+\gamma_2 P)$, a process enhanced by PKM2 activation. They do not proliferate in this model and they decay naturally at rate $\mu_M M$. As assumed in Macnamara and Eftimie [23], we assume that the memory cells persist for a very long time (compared to the effector and tumor cells), and thus we ignore their natural death rate. This was also assumed in other papers modeling memory CD8T cells in acute influenza [22], and such an idea is also supported in biological sense, as T cell memory declines slowly with a half-life of 8–15 years [24]. In addition, persistent tumor antigen drives antigen-dependent recruitment of MPECs back into the effector pool through the term $\frac{p_M T}{h_{M,T}+T} M$ [22], which represents the antigen-dependent reactivation of memory CD8$^+$ T-cells into effector cells. In this term, $d_{E,M}$ represents the maximum rate at which memory cells are recruited back into the effector pool, while the Michaelis-Menten factor $\frac{T}{h_{M,T}+T} M$ models the stimulation by tumor antigen where $h_{M,T}$ is the tumor burden at which the reactivation rate reaches one-half of its maximum value. While they do not directly kill tumor cells, they serve as long-lived reservoir that sustains effector responses over time and supports long term immune surveillance [25]. While most models will treat MPECs as the stage before the cells become long-lived memory cells [22], [20], our model chooses to opt out of having two compartments and chooses the one compartment MPEC instead. Inherent in this simplification is the assumption that all MPECs differentiate into long-lived memory cells. Biologically, however, MPECs preferentially survive the contraction phase and possess the potential to generate long-lived memory T cells, although experimental evidence suggests that not all MPECs ultimately populate the memory pool [25], [26].

IFN-γ (F):

$$\frac{dF}{dt} = p_{E,F} \frac{T}{h_{F,T}+T} E + p_{F,S} \frac{T}{h_{F,T}+T} S - \mu_F F \tag{10}$$

Equation (10) models IFN-γ production by activated CD8 T cell subsets in response to tumor antigen. Effector cells and short-lived effector cells contribute to cytokine secretion [25] [26]. ECs contribute through the antigen-dependent term $p_{E,F} \frac{T}{h_{F,T}+T} E$ adapted from Yu et al. [10] and we assume a similar mechanism of IFN-γ secretion by short-lived effector cells (SLECs) through the term $p_{F,S} \frac{T}{h_{F,T}+T} S$. These Michaelis-Menten forms capture the saturating nature of cytokine production and reflect the limited capacity of effector cells to increase IFN-γ output as tumor grows. IFN-γ goes through natural decay through the term $\mu_F F$.

Model 2:

$$\frac{dT}{dt} = (\alpha T^{2/3} - \beta T) - \delta_E \frac{(\frac{E}{T})^\lambda}{s + (\frac{E}{T})^\lambda} T(1 + \gamma_1 P) - \delta_F \frac{T}{h_{T,F} + T} F - \delta_S \frac{T}{h_{T,S} + T} S, \tag{11a}$$

$$\frac{dE}{dt} = \frac{pT}{h_{E,T} + T} E - \mu_E E^2 - d_{E,S} E(1 - \gamma_1 P) - d_{E,M} E(1 + \gamma_2 P) + \frac{p_M T}{h_{M,T} + T} M - \frac{c_T T E}{1 + \gamma_3 P}, \tag{11b}$$

$$\frac{dS}{dt} = d_{E,S} E(1 - \gamma_1 P) + \rho_S T S - \mu_{SS} S^2 - \mu_S S, \tag{11c}$$

$$\frac{dM}{dt} = d_{E,M} E(1 + \gamma_2 P) - \mu_M M - \frac{p_M T}{h_{M,T} + T} M, \tag{11d}$$

$$\frac{dF}{dt} = p_{F,E} \frac{T}{h_{F,T} + T} E + p_{F,S} \frac{T}{h_{F,T} + T} S - \mu_F F. \tag{11e}$$

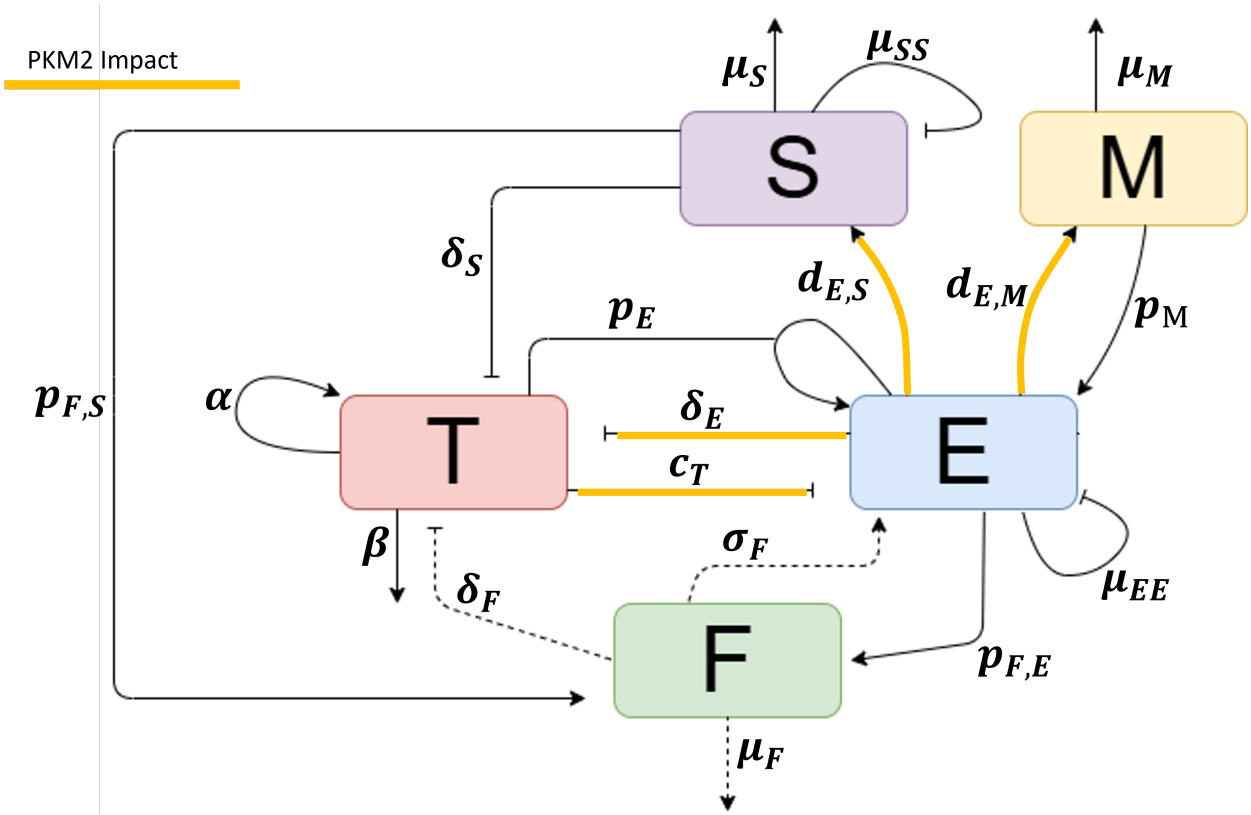


Figure 3: Interaction network of the tumor (T), effector CD8$^+$ T-cels (E), short-lived effector cells (S), memory precursor effector cells (M), and IFN-γ (F) populations for Model 2 given in System (11). Solid arrows denote cell-to-cell proliferation, activation, differentiation and production processes; dashed arrows denote cytokine mediated effects, and blunt ended arrows denote killing and inhibition. Parameter labels identify the rates associated with each process. The associated parameter descriptions are given in Table 5.

Parameter	Description	Units
Tumor Dynamics		
α	Von Bertalanffy tumor growth coefficient	tumor cells$^{1/3}$ h^{-1}
β	Tumor loss/death coefficient	h^{-1}
δ_E	Maximum EC-mediated tumor killing rate	h^{-1}
s	Saturation constant for the effector-to-tumor ratio $(E/T)^\lambda$	dimensionless
λ	Hill coefficient for EC-mediated tumor killing	dimensionless
δ_F	IFN-γ-mediated tumor killing coefficient	tumor cells $\cdot$ (pg/ml)$^{-1}$ h^{-1}
$h_{T,F}$	Tumor half-saturation constant for IFN-γ-mediated killing	tumor cells
δ_S	SLEC-mediated tumor killing coefficient	tumor cells $\cdot$ SLEC^{-1} h^{-1}
$h_{T,S}$	Tumor half-saturation constant for SLEC-mediated killing	tumor cells
Effector CD8$^+$ T Cells (E)		
p	Maximum antigen-driven EC proliferation rate	h^{-1}
$h_{E,T}$	Tumor half-saturation constant for EC stimulation	tumor cells
μ_E	Density-dependent EC death coefficient	EC^{-1} h^{-1}
$d_{E,S}$	Differentiation rate from ECs to SLECs	h^{-1}
$d_{E,M}$	Differentiation rate from ECs to MPECs	h^{-1}
c_T	Tumor-induced EC exhaustion/death coefficient	tumor cells^{-1} h^{-1}
Short-Lived Effector Cells (SLECs)		
ρ_S	Tumor-stimulated SLEC expansion coefficient	tumor cells^{-1} h^{-1}
μ_{SS}	Density-dependent SLEC death coefficient	SLEC^{-1} h^{-1}
μ_S	Natural SLEC death rate	h^{-1}
Memory Precursor Effector Cells (MPECs)		
μ_M	Natural MPEC death rate	h^{-1}
p_M	Antigen-driven reactivation rate from MPECs to ECs	h^{-1}
$h_{M,T}$	Tumor half-saturation constant for MPEC reactivation	tumor cells
IFN-γ Dynamics		
$p_{F,E}$	IFN-γ production rate by antigen-stimulated ECs	(pg/ml) $\cdot$ EC^{-1} h^{-1}
$p_{F,S}$	IFN-γ production rate by antigen-stimulated SLECs	(pg/ml) $\cdot$ SLEC^{-1} h^{-1}
$h_{F,T}$	Tumor half-saturation constant for IFN-γ production	tumor cells
μ_F	IFN-γ decay rate	h^{-1}
PKM2 / TEPP46 Effects		
P	Normalized PKM2 activation level induced by TEPP46 treatment	dimensionless
γ_1	PKM2 effect on tumor killing and EC-to-SLEC differentiation	dimensionless
γ_2	PKM2 enhancement of EC-to-MPEC differentiation	dimensionless

Table 5: Model parameters, descriptions, and dimensional units for Model 2 (Tumor-Immune-Memory Model) with PKM2 treatment presented in System (6)-(10).

3 Model 4: Intracellular-Microenvironment Model

The framework of this model consists of two relatively independent yet dynamically coupled submodels: a micro-scale submodel (Submodel 1) that simulates the intracellular glucose metabolic network and PKM2 conformational dynamics within a single effector T cell, and a macro-scale submodel (Submodel 2) that captures population dynamics, nutrient competition, and lactate-mediated immunosuppression in the tumor microenvironment (TME). Table 6 lists all dynamic state variables involved in both the macro-scale microenvironment and the micro-scale intracellular compartments. Table 7 summarizes the newly introduced intracellular metabolic parameters and the microenvironmental metabolic competition parameters.

Variable	Biological Description
Macro-scale Variables	
$T(t)$	Population density of tumor cells
$E(t)$	Population density of effector T cells
$F(t)$	Concentration of cytokines (e.g., IFN-γ) in the TME
$G(t)$	Concentration of extracellular glucose in the TME
$L(t)$	Concentration of accumulated lactate in the TME
Micro-scale Variables (Inside an Effector T Cell)	
$G_{in}(t)$	Concentration of intracellular free glucose
$P_{act}(t)$	Proportion of PKM2 in the highly active tetrameric state ($0 \leq P_{act} \leq 1$)
$A(t)$	Intracellular ATP (energy) level

Table 6: System Variables of the Multi-scale Model given in System (12)-(20).

Parameter	Description	Units
Micro-scale Metabolic & PKM2 Parameters		
v_{import}	Maximum rate of extracellular glucose uptake by T cells	Conc.* $\cdot$ h^{-1}
$h_{G,E}$	Half saturation constant of glucose intake of effector cells	Conc.
k	Rate constant of intracellular glucose consumption	h^{-1}
χ_0	Basal activation rate of PKM2	h^{-1}
χ_1	Efficacy of the TEPP in activating PKM2	Conc.$^{-1}$ $\cdot$ h^{-1}
μ_P	Natural decay rate of PKM2 tetramers	h^{-1}
P	Concentration of TEPP treatment	Conc.
θ_{gly}	ATP yield from dimer-driven aerobic glycolysis	Dimensionless
θ_{ox}	ATP yield from tetramer-driven OXPHOS ($\theta_{ox} \gg \theta_{gly}$)	Dimensionless
a_O	Relative glucose utilization coefficient of oxidative tumor cells	Dimensionless
a_W	Relative glucose utilization coefficient of glycolytic tumor cells	Dimensionless
Macro-scale Microenvironmental Parameters		
α_O	Intrinsic growth capacity of oxidative tumor cells	$cells^{1/3} \cdot h^{-1}$
α_W	Intrinsic growth capacity of glycolytic (Warburg) tumor cells	$cells^{1/3} \cdot h^{-1}$
$h_{A,E}$	Half saturation constant of intracellular ATP availability for effector cells	Conc.
η_L	Strength of lactate-induced immunosuppression	Conc.
$h_{A,x}$	Half-inhibitory constant of ATP availability for resisting T cell exhaustion.	Conc.
$h_{A,F}$	Half saturation constant of the enhancement of ATP on IFN-γ secretion	Conc.
v_T	Maximum glucose consumption rates per tumor cell	Conc. $\cdot$ Cell^{-1} $\cdot$ h^{-1}
$h_{G,T}$	Half saturation constant of glucose intake of tumor cells	Conc.
μ_G	Natural decay rate of glucose	h^{-1}
r_T	Yield of lactate from consumed glucose from tumor cells	Dimensionless
r_E	Yield of lactate from consumed glucose from effector cells	Dimensionless
μ_L	Natural decay rate of lactate	h^{-1}

* unit for concentration. pg/ml

Table 7: Metabolic and PKM2 Dynamic parameters descriptions of the model given in System (12)-(20).

3.0.1 Submodel 1: Microscopic Intracellular Metabolism and PKM2 Regulation

This submodel tracks the metabolic reprogramming within a typical effector CD8$^+$ T cell.

1. Intracellular Glucose Dynamics (G_{in})

$$\frac{dG_{in}}{dt} = v_{import}\left(\frac{G}{h_{G,E}+G}\right) - k \cdot G_{in} \tag{12}$$

Equation (12) is based on the demonstration by Jeon et al. (2018) [27] that intracellular enzymatic networks follow Michaelis-Menten kinetics. We extended this mathematical rationale to the trans-membrane import process, using the saturation term $\left(\frac{G}{h_{G,E}+G}\right)$ to model the limited capacity of Glucose transporters (GLUT) when extracellular glucose (G) is abundant. v_{import} is then the maximum glucose import rate for a typical effector CD8$^+$T cell. k is the consumption rate of intracellular glucose.

2. PKM2 Conformational Dynamics (P_{act})

$$\frac{dP_{act}}{dt} = (\chi_0 + \chi_1 P)(1 - P_{act}) - \mu_P P_{act} \tag{13}$$

Equation (13) is a two-state transition model constructed using the classic Law of Mass Action. χ_0 is the basal activation rate of PKM2. The PKM2-targeted activator (P) forces the low-activity dimers ($1 - P_{act}$) to polymerize into high-activity tetramers (P_{act}) at a rate $\chi_1 P$.

3. Intracellular Energy (ATP) Generation (A)

$$\frac{dA}{dt} = \left[\theta_{gly}(1 - P_{act}) + \theta_{ox} P_{act}\right] k \cdot G_{in} - \mu_A A \tag{14}$$

This equation (14) translates the metabolic reprogramming mechanisms reviewed by Farsani et al. [7]. The PKM2 dimer state directs carbon flux to aerobic glycolysis (low ATP yield, $\theta_{gly}(1 - P_{act})$), whereas the tetramer state redirects flux into mitochondrial oxidative phosphorylation (high ATP yield, $\theta_{ox} P_{act}$).

3.0.2 Submodel 2: Macroscopic TME Population Dynamics

1. Tumor Cell Dynamics (T)

$$\frac{dT}{dt} = \left[\alpha_O \phi_O(L) + \alpha_W \phi_W(L)\right] T^{2/3} - \beta T - \delta_E \frac{A}{h_{A,E}+A} S_L(L) \frac{(E/T)^\lambda}{s + (E/T)^\lambda} T - \delta_F \frac{T}{h_{T,F}+T} F \tag{15}$$

Equation (15) models the dynamic of the tumor cell population while accounting for the different metabolic phenotypes. Tumor growth is represented by the term $\left[\alpha_O \phi_O(L) + \alpha_W \phi_W(L)\right] T^{2/3} - \beta T$ where α_O and α_W characterize the intrinsic growth capacity of oxidative and glycolytic tumor cells respectively. The functions $\phi_W(L)$ and $\phi_O(L)$, adopted from Mendoza-Juez et al. (2012) [28], describe the fractions of oxidative and glycolytic tumor cells as functions of extracellular lactate concentration L. We assume that extracellular lactate acts as a metabolic feedback signal, with increasing lactate promoting a shift from glycolytic to oxidative metabolism. This assumption is motivated by Xie et al. (2014) [29], who proved through experimental observation that lactate accumulation and lactic acidosis reduce glycolytic activity and promote a more oxidative state in cancer cells. Since extracellular pH is not explicitly modeled, lactate concentration is used as a proxy for lactic acidosis. Previous mathematical models such as Mendoza-Juez et al. (2012) [28] have used lactate as a regulator of the balance between glycolytic and oxidative tumor populations. $\delta_E \frac{A}{h_{A,E}+A} S_L(L) \frac{(E/T)^\lambda}{s+(E/T)^\lambda} T$ describes direct tumor killing by effector CD8$^+$ T cells. The factor $\frac{A}{h_{A,E}+A}$ is a Michaelis-Menten function that represents the dependence of T-cells on intracellular ATP availability. The variable A represents the concentration of ATP within activated CD8$^+$ T cells, serving as a measure of their metabolic fitness. The parameter $h_{A,E}$ is the half saturation constant and it denotes the ATP concentration at which effector cell-mediated killing reaches one half its maximal value. This assumes that highly energetic T cells possess greater cytotoxic potential, while ATP-limited cells exhibit reduced effector function. The factor $S_L(L)$ represents lactate-mediated immunosuppression where $S_L(L) = \frac{1}{1+\eta_L L}$ and η_L quantifies the strength of lactate-induced immunosuppression.

2. Effector T Cell Dynamics (E)

$$\frac{dE}{dt} = \frac{T}{h_{E,T}+T}E(p_E + \sigma_F F) - d_{E,M}(J_{\text{gly},E})E - c_T TE \cdot \frac{h_{A,x}}{h_{A,x}+A} - \mu_E E + \frac{p_M T}{h_{M,T}+T}M \tag{16}$$

In Equation (16), the inhibition effect of PKM2 activation on the exhaustion of CD8T cells is now modeled by the term $\frac{h_{A3}}{h_{A3}+A}$. We make the assumption based on Farsani et al. (2025) [7] who claimed that the activation of PKM2 enhances mitochondrial function, enabling T cells to produce more ATP. This abundant supply of ATP subsequently slows down T cell exhaustion.

3. Cytokine Dynamics (F)

$$\frac{dF}{dt} = p_F E \frac{A}{h_{A,F}+A} S_L(L) - \mu_F F \tag{17}$$

ATP is a positive regulator of T cell function, in Equation (17) the Michaelis-Menten term $\frac{A}{h_{A,F}+A}$ assumes that IFN-γ secretion is energetically demanding and therefore depends on intracellular ATP availability. As ATP levels increase, effector T cells gain a greater capacity to produce cytokines [30], whereas ATP-depleted cells exhibit impaired function. In contrast $S_L(L)$ accounts for lactate-mediated immunosuppression. Where $S_L(L) = \frac{1}{1+\eta_L L}$ and η_L denotes the strength of lactate-induced immunosuppression.

4. Memory CD 8^+ T Cell Dynamic (M)

$$\frac{dM}{dt} = d_{E,M}(J_{\text{gly},E})E - \mu_M M - \frac{p_M T}{h_{M,T}+T}M \tag{18}$$

Memory cells are modeled as long-lived population generated from activated $CD8^+$ T cells. Experimentally observed data have shown a relationship between T-cell metabolism and memory differentiation [31], [32], [7], where excessive glycolytic activity promotes terminal effector differentiation while moderate glycolytic activity favors memory precursor formation [31]. We define the effective glycolytic flux as

$$J_{\text{gly}} = (1 - P_{\text{act}})kG_{\text{in}}$$

where P_{act} denotes the fraction of PKM2 in the active tetrameric state, G_{in} is the intracellular glucose concentration, and kG_{in} represents glucose processing. The idea is that through its regulation of glycolytic metabolism, PKM2 indirectly controls memory differentiation. We modify the differentiation rate to become

$$d_{E,M} = d_{E,M}^{\max} \exp\left\{-\frac{(J_{\text{gly}} - J_{\text{opt}})^2}{2\sigma_J^2}\right\}.$$

Here, $d_{E,M}^{\max}$ is the maximum differentiation rate, J_{opt} represents the glycolytic flux associated with optimal memory precursor generation, and σ_J controls the range of glycolytic fluxes that support memory differentiation. This Gaussian formulation assumes that memory formation is maximized at an intermediate state. When glycolytic flux exceeds J_{opt}, effector cells preferentially opt for a terminal effector phenotype, and very low glycolytic flux reflects insufficient metabolic activity to support efficient memory cell generation [32].

5. Glucose Dynamics (G)

$$\frac{dG}{dt} = S_G - v_T T[a_O\phi_O(L) + a_W\phi_W(L)](\frac{G}{h_{G,T}+G}) - v_{import}E(\frac{G}{h_{G,E}+G}) - \mu_G G \tag{19}$$

Equation (19) describes extracellular glucose dynamic within the tumor microenvironment. Glucose enters the system through constant vascular supply represented by S_G. Glucose is consumed by tumor cells through the term $v_T T\big[a_O\phi_O(L) + a_W\phi_W(L)\big]\big(\frac{G}{h_{G,T}+G}\big)$. The parameter v_T denotes the maximum glucose consumption per tumor cell while a_O and a_W represent the relative glucose utilization rates of oxidative and glycolytic tumor phenotypes, respectively, allowing glycolytic tumor cells to consume glucose at a higher rate than oxidative tumor cells. The switch functions Mendoza-Juez et al. (2012) [28] $\phi_O(L)$ and $\phi_W(L)$ determine the fraction of tumor cells in each metabolic state. Glucose uptake is assumed to follow Michaelis-Menten kinetics through the factor $\frac{G}{h_{G,T}+G}$, where $h_{G,T}$ is the glucose half-saturation constant for tumor

cells and represents the glucose concentration at which tumor glucose uptake reaches one-half of its maximal value. This formulation has been widely employed in mathematical models of tumor metabolism and tumor immune interactions [28], [33], [30]. $CD8^+$ T cells also consume glucose through the term $v_{import}E(\frac{G}{h_{G,E}+G})$. v_{import} represents the maximum glucose uptake rate of activated effector cells while $h_{G,E}$ is the glucose half-saturation constant for T-cell glucose uptake. Together, the tumor and effector cell glucose uptake terms represent competitive consumption of a shared metabolic resource within the tumor microenvironment. Both populations depend on the same extracellular glucose pool, and their uptake rates are governed by saturating Michaelis-Menten kinetics. This formulation captures the metabolic competition paradigm described by Frades et al. (2021) [21], in which tumor cells and immune cells compete for limited nutrients, and increased glucose consumption by one population reduces nutrient availability for the other.

6. Lactate Dynamic (L)

$$\frac{dL}{dt} = r_T v_T T a_W \phi_W(L)(\frac{G}{h_{G,T}+G}) + r_E \theta_{gly}(1-P_{act})kG_{in} - \mu_L L \tag{20}$$

Equation (20) describes the dynamic of extracellular lactate within the tumor microenvironment. Lactate is produced by glycolytic tumor cells through the term $r_T v_T T a_W \phi_W(L)(\frac{G}{h_{G,T}+G})$. The parameter r_T denotes the amount of lactate produced per glucose consumed. Since lactate is primarily generated through aerobic glycolysis, only the glycolytic fraction of the tumor population contributes to lactate production as represented by the factor $a_W\phi_W(L)$ [28]. The Michaelis-Menten term $\frac{G}{h_{G,T}+G}$ reflects the dependence of lactate production on glucose availability. This is directly adapted from the systemic modeling of the Warburg phenotype by Spinicci et al. (2022) [34]. Activated $CD8^+$ T cells provide an additional source of lactate through the term $r_E\theta_{gly}(1-P_{act})kG_{in}$. In this equation, r_E represents the lactate yield associated with glycolytic metabolism in activated T cells, θ_{gly} denotes the ATP yield associated with PKM2 dimer-driven glycolytic metabolism. The factor $(1-P_{act})$ represents the fraction of PKM2 remaining in the dimeric state. Lactate production is greatest when PKM2 remains in the dimeric state which is associated with the glycolytic phenotype and enhanced lactate generation.

7. Switch Functions

$$\phi_O(L) = \frac{1}{2}[1+\tanh(\beta_L(L-L_c))] \tag{21}$$

$$\phi_W(L) = 1-\phi_O(L) \tag{22}$$

Full Intracellular-Microenvironment Model:

$$\frac{dG_{in}}{dt} = v_{import}\left(\frac{G}{h_{G,E}+G}\right) - k\cdot G_{in} \tag{23a}$$

$$\frac{dP_{act}}{dt} = (\chi_0+\chi_1 P)(1-P_{act}) - \mu_P P_{act} \tag{23b}$$

$$\frac{dA}{dt} = [\theta_{gly}(1-P_{act})+\theta_{ox}P_{act}]\,k\cdot G_{in} - \mu_A A \tag{23c}$$

$$\frac{dT}{dt} = [\alpha_O\phi_O(L)+\alpha_W\phi_W(L)]\,T^{2/3} - \beta T - \delta_E\frac{A}{h_{A,E}+A}S_L(L)\frac{(E/T)^\lambda}{s+(E/T)^\lambda}T - \delta_F\frac{T}{h_{T,F}+T}F \tag{23d}$$

$$\frac{dE}{dt} = \frac{T}{h_{E,T}+T}E(p_E+\sigma_F F) - d_{E,M}(J_{\mathrm{gly},E})E - c_T T E\cdot\frac{h_{A,x}}{h_{A,x}+A} - \mu_E E + \frac{p_M T}{h_{M,T}+T}M \tag{23e}$$

$$\frac{dF}{dt} = p_F E\frac{A}{h_{A,F}+A}S_L(L) - \mu_F F \tag{23f}$$

$$\frac{dM}{dt} = d_{E,M}(J_{\mathrm{gly},E})E - \mu_M M - \frac{p_M T}{h_{M,T}+T}M \tag{23g}$$

$$\frac{dG}{dt} = S_G - v_T T[a_O\phi_O(L)+a_W\phi_W(L)](\frac{G}{h_{G,T}+G}) - v_{import}E(\frac{G}{h_{G,E}+G}) - \mu_G G \tag{23h}$$

$$\frac{dL}{dt} = r_T v_T T a_W \phi_W(L)\left(\frac{G}{h_{G,T}+G}\right) + r_E \theta_{gly}(1-P_{act})kG_{in} - \mu_L L \tag{23i}$$

Corresponding chemical equation (Conservation of carbon):

$$C_6H_{12}O_6 \text{ (Glucose)} \rightarrow 2C_3H_6O_3 \text{ (Lactate)}$$

Theoretical yield: A single glucose molecule, containing 6 carbon atoms, is cleaved exactly in half to produce two lactate molecules, each containing 3 carbon atoms. Therefore, regardless of whether it is a tumor cell or a T cell, as long as it utilizes the glycolytic pathway, its theoretical stoichiometric yield is $r_T = 2$ and $r_E = 2$.

4 Results

4.1 Data Fitting: Tumor Growth Dynamics

We fit the 6 candidate tumor growth models described in Table 1 to each of the six B16-F10 melanoma datasets and compared their performance using AICc. The resulting parameter estimates, model rankings and fit visualizations are presented below, followed by a summary and biological interpretation of the overall fitting results.

4.1.1 Dataset 1

Fitting the six models in Table 1 to B16-F10 tumor growth data in N.S. mice provided in dataset 1 [12] lead to the Von Bertalanffy 1 model being the best fit, with the smallest AICc value of -26.7499, followed by the Gompertz 1 and 2 models, with an AICc of -19.2453 (See Table 8). We estimated the growth parameters for the Von Bertalanffy model to be $\alpha = 2.3145 \times 10^1 cells^{\frac{1}{3}} h^{-1}$ and $\beta = 1.6554 \times 10^{-2}\ h^{-1}$. The resulting parameter estimates and AICc values for the six growth models are reported in Table 8. The model best fit solutions are plotted along with the data in Figure 4.

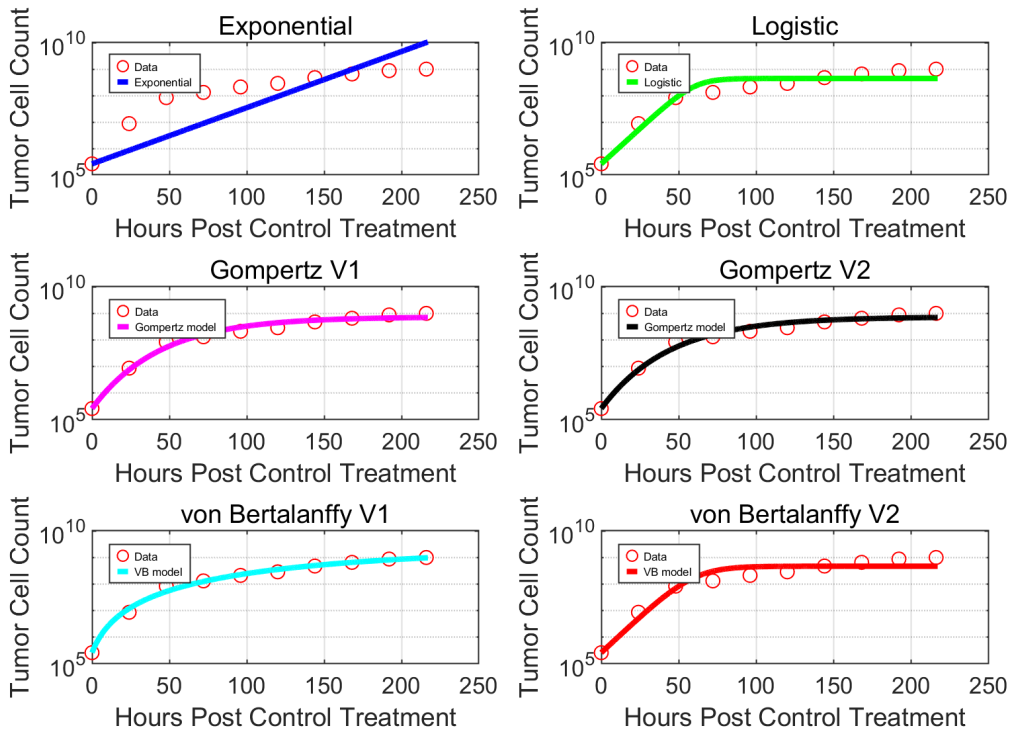


Figure 4: Data fitting results (Dataset 1): Datapoints from day 5 to 14 (red circles) [12] are fit to the tumor growth (solid lines) models listed in Table 1. Best fit parameters for each model is given in Table 8.

Model	**Equation**	**Parameters(Unit)**	**fval (SSE)**	**k**	**AICc**
Logistic	$\frac{dT}{dt} = rT\left(1 - \frac{T}{K}\right)$	$r = 1.2353 \times 10^{-1}\ h^{-1}$ $K = 4.4741 \times 10^{8}\ cells*$	3.3114×10^{0}	2	-5.3379
Exponential	$\frac{dT}{dt} = rT$	$r = 4.8938 \times 10^{-2}\ h^{-1}$	3.7086×10^{1}	1	15.6065
Gompertz 1	$\frac{dT}{dt} = G_0 e^{-\alpha t} T$	$G_0 = 1.8206 \times 10^{-1}\ h^{-1}$ $\alpha = 2.2897 \times 10^{-2}\ h^{-1}$	8.2418×10^{-1}	2	-19.2453
Gompertz 2	$\frac{dT}{dt} = aT\ln\left(\frac{1}{bT}\right)$	$a = 2.2891 \times 10^{-2}\ h^{-1}$ $b = 1.3393 \times 10^{-9}\ cells^{-1}$	8.2418×10^{-1}	2	-19.2453
Von Bertalanffy 1	$\frac{dT}{dt} = \alpha T^{2/3} - \beta T$	$\alpha = 2.3145 \times 10^{1}\ cells^{\frac{1}{3}} h^{-1}$ $\beta = 1.6554 \times 10^{-2}\ h^{-1}$	3.8913×10^{-1}	2	**-26.7499**
Von Bertalanffy 2	$\frac{dT}{dt} = \alpha T((\beta T)^{2/3} - 1)$	$\alpha = -1.2635 \times 10^{-1}\ h^{-1}$ $\beta = 2.1094 \times 10^{-9}\ cells^{-1}$	2.8479×10^{0}	2	-6.8457

* the unit “cells" stands for number of tumor cells

Table 8: Best fit parameters and model comparison from fitting Dataset 1 [12] to six tumor growth models in Table 1. The corresponding solution to each model is presented in Figure 4. The AICc is calculated as $AIC_c = n\ln\left(\frac{SSE}{n}\right) + 2k + \frac{2k(k+1)}{n-k-1}$. The smallest AICc value is bolded.

4.1.2 Dataset 2

Fitting the six models in Table 1 to B16-F10 tumor growth data in N.S. mice with IL-2gR knocked out provided in dataset 2 [14] lead to the Exponential model being the best fit, with the smallest AICc value of -11.2654, followed by the Logistic model, with an AICc of -7.7248 (See Table 9). The Logistic model is considered to be equivalent to the best fit because the difference between their AICc value is ≤ 4. We estimated the growth parameters for the Exponential model to be $r = 2 \times 10^{-2}\ h^{-1}$. The resulting parameter estimates and AICc values for the six growth models are reported in Table 9. The model best fit model solutions are plotted along with the data in Figure 5.

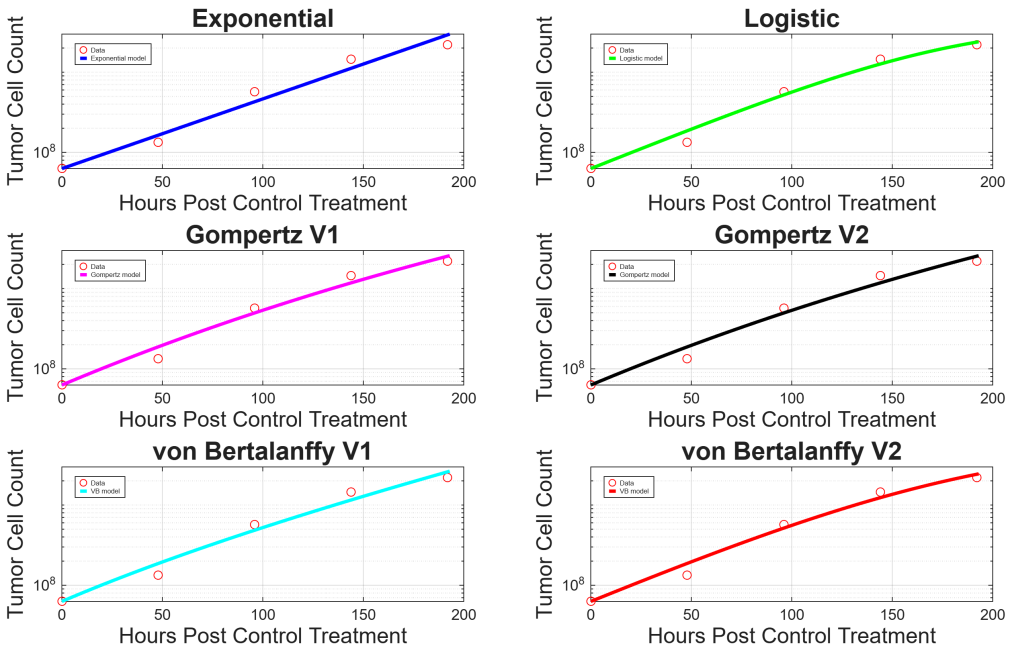


Figure 5: Data fitting results (Dataset 2): Datapoints from day 1 to 5 (red circles) [14] are fit to the tumor growth (solid lines) models listed in Table 1. Best fit parameters for each model is given in Table 9.

Model	Equation	Parameters(Unit)	log-SSE	k	AICc
Logistic	$\frac{dT}{dt} = rT(1 - \frac{T}{K})$	$r = 2.3265 \times 10^{-2}\ h^{-1}$ $K = 2.421 \times 10^{10} cells$	1.4434×10^{-1}	2	-7.7248
Exponential	$\frac{dT}{dt} = rT$	$r = 2 \times 10^{-2}\ h^{-1}$	$2.697325e \times 10^{-1}$	1	**-11.2654**
Gompertz 1	$\frac{dT}{dt} = G_0 e^{-\alpha t} T$	$G_0 = 2.4247 \times 10^{-2}\ h^{-1}$ $\alpha = 2.498198 \times 10^{-3}\ h^{-1}$	1.991981×10^{-1}	2	-6.1145
Gompertz 2	$\frac{dT}{dt} = aT \ln(\frac{1}{bT})$	$a = 2.478 \times 10^{-2}\ h^{-1}$ $b = 2.4210 \times 10^{-10}\ cells^{-1}$	1.991832×10^{-1}	2	-6.1148
Von Bertalanffy 1	$\frac{dT}{dt} = \alpha T^{2/3} - \beta T$	$\alpha = 4.630792\ cells^{\frac{1}{3}} h^{-1}$ $\beta = -1.297729 \times 10^{-2}\ h^{-1}$	2.170911×10^{-1}	2	-5.6844
Von Bertalanffy 2	$\frac{dT}{dt} = \alpha T((\beta T)^{2/3} - 1)$	$\alpha = -2.44 \times 10^{-2}\ h^{-1}$ $\beta = 9.137866 \times 10^{-13}\ cells^{-1}$	1.607766×10^{-1}	2	-7.1859

Table 9: Best fit parameters and model comparison from fitting Dataset 2 [14] to six tumor growth models in Table 1. The corresponding solution to each model is presented in Figure 5. The AICc is calculated as $AIC_c = n \ln\left(\frac{SSE}{n}\right) + 2k + \frac{2k(k+1)}{n-k-1}$. The smallest AICc value is bolded.

4.1.3 Dataset 3

Fitting the six models in Table 1 to B16-F10 tumor growth data in SCID mice provided in dataset 3 [15] lead to the Exponential model being the best fit, with the smallest AICc value of -24.9034, followed by the Von Bertalanffy 1 model, with an AICc of -23.8269 (See Table 10). We estimated the growth parameters for the Von Bertalanffy 1 model to be $\alpha = 10.489863\ cells^{\frac{1}{3}} h^{-1}$ and $\beta = 1.300590 \times 10^{-3}\ h^{-1}$. Moreover, for dataset 3, all models are considered to be equivalent to the best fit as the difference between their AICc value and the minimum AICc value is $\leq$ to 4. The resulting parameter estimates and AICc values for the six growth models are reported in Table 10. The model best fit model solutions are plotted along with the data in Figure 6.

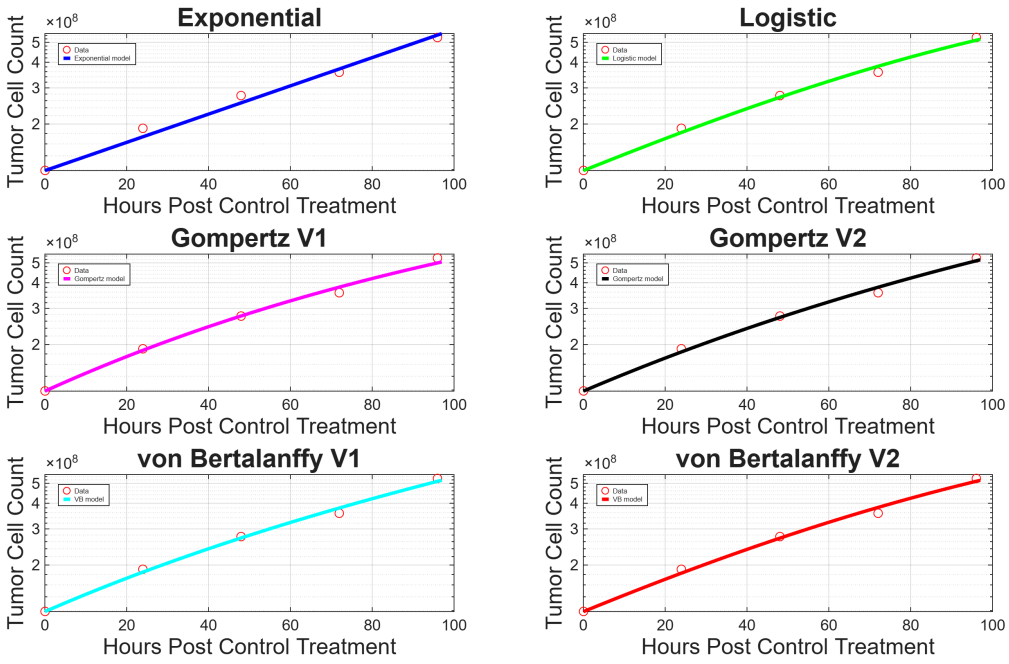


Figure 6: Data fitting results (Dataset 3): Datapoints from day 12 to 16 (red circles) [15] are fit to the tumor growth (solid lines) models listed in Table 1. Best fit parameters for each model is given in Table 10.

Model	**Equation**	**Parameters**	**log-SSE**	**k**	**AICc**
Logistic	$\frac{dT}{dt} = rT(1 - \frac{T}{K})$	$r = 2.0678 \times 10^{-2}\ h^{-1}$ $K = 9.205086 \times 10^{10} cells$	8.053089×10^{-3}	2	-22.1557
Exponential	$\frac{dT}{dt} = rT$	$r = 1.5859 \times 10^{-2}\ h^{-1}$	1.763442×10^{-2}	1	**-24.9034**
Gompertz 1	$\frac{dT}{dt} = G_0 e^{-\alpha t} T$	$G_0 = 2.80842 \times 10^{-2}\ h^{-1}$ $\alpha = 7.280267 \times 10^{-3}\ h^{-1}$	7.425630×10^{-3}	2	-22.5613
Gompertz 2	$\frac{dT}{dt} = aT \ln(\frac{1}{bT})$	$a = 5.458 \times 10^{-3}\ h^{-1}$ $b = 2.335917 \times 10^{-10}\ cells^{-1}$	6.289347×10^{-3}	2	-23.3917
Von Bertalanffy 1	$\frac{dT}{dt} = \alpha T^{2/3} - \beta T$	$\alpha = 10.489863\ cells^{\frac{1}{3}} h^{-1}$ $\beta = 1.300590 \times 10^{-3}\ h^{-1}$	5.765085×10^{-3}	2	-23.8269
Von Bertalanffy 2	$\frac{dT}{dt} = \alpha T \left((\beta T)^{2/3} - 1\right)$	$\alpha = -2.3372 \times 10^{-2}\ h^{-1}$ $\beta = 7.389298 \times 10^{-10}\ cells^{-1}$	7.443581×10^{-3}	2	-22.5492

Table 10: Best fit parameters and model comparison from fitting Dataset 3 [15] to six tumor growth models in Table 1. The corresponding solution to each model is presented in Figure 6. The AICc is calculated as $AIC_c = n \ln\left(\frac{SSE}{n}\right) + 2k + \frac{2k(k+1)}{n-k-1}$. The smallest AICc value is bolded.

4.1.4 Dataset 4

Fitting the six models in Table 1 to B16-F10 tumor growth data in SCID mice provided in dataset 4 [16] lead to the Gompertz 1 model being the best fit, with the smallest AICc value of -62.5838, followed by the Von Bertalanffy 1 model, with an AICc of -60.8528 (See Table 11). The Von Bertalanffy 1 model is considered to be equivalent to the best fit because the difference between their AICc value is $\leq$ to 4. We estimated the

growth parameters for the Gompertz 1 model to be $G_0 = 2.45 \times 10^{-3}\ h^{-1}$ and $\alpha = -5.715086 \times 10^{-3}\ h^{-1}$. The resulting parameter estimates and AICc values for the six growth models are reported in Table 11. The model best fit model solutions are plotted along with the data in Figure 7.

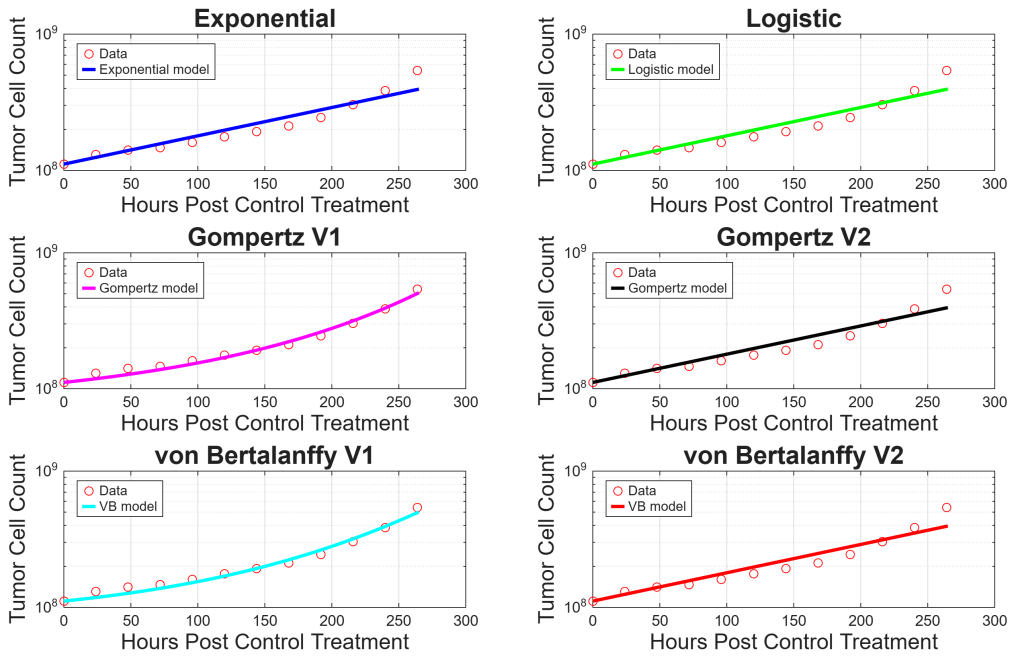


Figure 7: Data fitting results (Dataset 4): Datapoints from day 0 to 12 (red circles) [16] are fit to the tumor growth (solid lines) models listed in Table 1. Best fit parameters for each model is given in Table 11.

Model	**Equation**	**Parameters**	**log-SSE**	**k**	**AICc**
Logistic	$\frac{dT}{dt} = rT(1 - \frac{T}{K})$	$r = 4.786 \times 10^{-3}\ h^{-1}$ $K = 2.847601 \times 10^{25} cells$	2.038930×10^{-1}	2	-43.5675
Exponential	$\frac{dT}{dt} = rT$	$r = 4.781 \times 10^{-3}\ h^{-1}$	2.039009×10^{-1}	1	-46.5003
Gompertz 1	$\frac{dT}{dt} = G_0 e^{-\alpha t} T$	$G_0 = 2.45 \times 10^{-3}\ h^{-1}$ $\alpha = -5.715086 \times 10^{-3}\ h^{-1}$	4.180023×10^{-3}	2	**-62.5838**
Gompertz2	$\frac{dT}{dt} = aT \ln(\frac{1}{bT})$	$a = 7.0 \times 10^{-6}\ h^{-1}$ $b = 5.562757 \times 10^{-309}\ cells^{-1}$	2.042518×10^{-1}	2	-43.5464
Von Bertalanffy 1	$\frac{dT}{dt} = \alpha T^{2/3} - \beta T$	$\alpha = -9.658052\ cells^{\frac{1}{3}} h^{-1}$ $\beta = -2.242498 \times 10^{-2}\ h^{-1}$	4.828652×10^{-2}	2	-60.8528
Von Bertalanffy2	$\frac{dT}{dt} = \alpha T \left((\beta T)^{2/3} - 1 \right)$	$\alpha = -4.786 \times 10^{-3}\ h^{-1}$ $\beta = 1.106206 \times 10^{-30}\ cells^{-1}$	2.038930×10^{-1}	2	-43.5675

Table 11: Best fit parameters and model comparison from fitting Dataset 4 [16] to six tumor growth models in Table 1. The corresponding solution to each model is presented in Figure 7. The AICc is calculated as $AIC_c = n \ln\left(\frac{SSE}{n}\right) + 2k + \frac{2k(k+1)}{n-k-1}$. The smallest AICc value is bolded.

4.1.5 Dataset 5

Fitting the six models in Table 1 to B16-F10 tumor growth data in N.S. mice provided in dataset 5 [17] lead to the Von Bertalanffy 1 model being the best fit, with the smallest AICc value of -26.6912, followed by the Gompertz 2 model, with an AICc of -20.3942 (See Table 12). We estimated the growth parameters for the Von Bertalanffy 1 model to be $\alpha = 1.3026 \times 10^{1}\ cells^{\frac{1}{3}}h^{-1}$ and $\beta = 3.5782 \times 10^{-3}\ h^{-1}$. The resulting parameter estimates and AICc values for the six growth models are reported in Table 12. The model best fit model solutions are plotted along with the data in Figure 8.

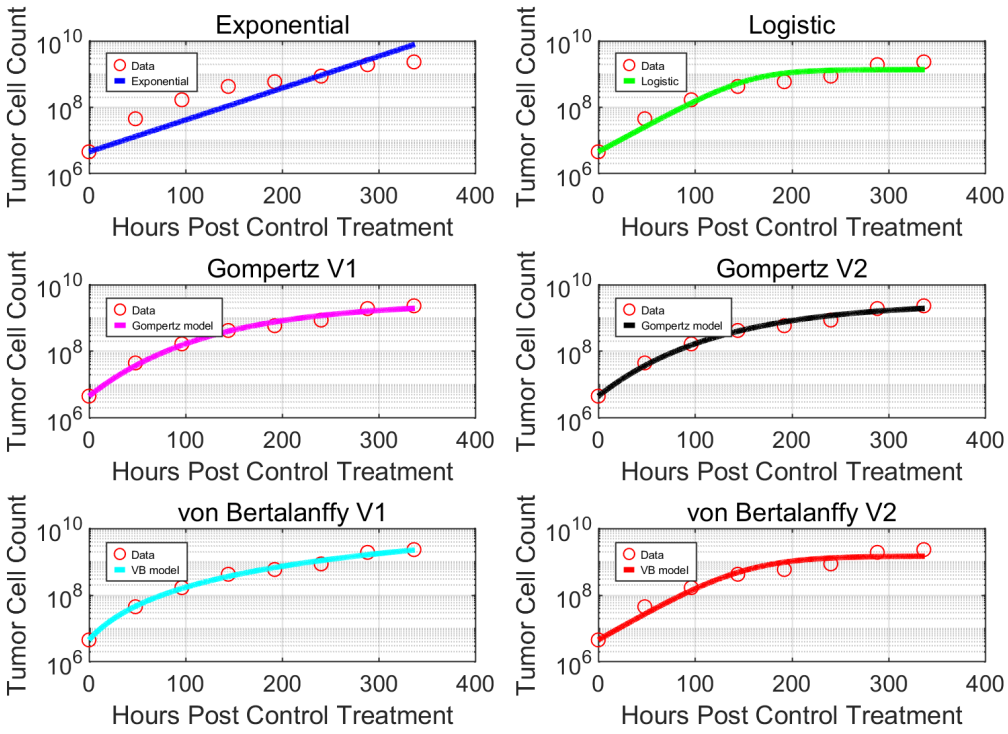


Figure 8: Data fitting results (Dataset 5): Datapoints from day 8 to 22 (red circles) [17] are fit to the tumor growth (solid lines) models listed in Table 1. Best fit parameters for each model is given in Table 12.

(Model)	Equation	(Parameters)	fval (SSE)	k	AICc
Logistic	$\frac{dT}{dt} = rT\left(1 - \frac{T}{K}\right)$	$r = 3.6237 \times 10^{-2}\ h^{-1}$ $K = 1.3593 \times 10^{9} cells$	1.3380×10^{0}	2	-7.9061
Exponential	$\frac{dT}{dt} = rT$	$r = 2.2120 \times 10^{-2}\ h^{-1}$	7.4555×10^{0}	1	2.1027
Gompertz 1	$\frac{dT}{dt} = G_0 e^{-\alpha t} T$	$G_0 = 5.2940 \times 10^{-2}\ h^{-1}$ $\alpha = 8.1801 \times 10^{-3}\ h^{-1}$	2.8088×10^{-1}	2	-20.3941
Gompertz 2	$\frac{dT}{dt} = aT\ln\left(\frac{1}{bT}\right)$	$a = 8.1890 \times 10^{-3}\ h^{-1}$ $b = -2.1801 \times 10^{1}\ cells^{-1}$	2.8088×10^{-1}	2	-20.3942
Von Bertalanffy 1	$\frac{dT}{dt} = \alpha T^{2/3} - \beta T$	$\alpha = 1.3026 \times 10^{1}\ cells^{\frac{1}{3}} h^{-1}$ $\beta = 3.5782 \times 10^{-3}\ h^{-1}$	1.2784×10^{-1}	2	**-26.6912**
Von Bertalanffy 2	$\frac{dT}{dt} = \alpha T((\beta T)^{2/3} - 1)$	$\alpha = -3.8713 \times 10^{-2}\ h^{-1}$ $\beta = -2.1122 \times 10^{1}\ cells^{-1}$	1.0275×10^{0}	2	-10.0184

Table 12: Best fit parameters and model comparison from fitting Dataset 5 [17] to six tumor growth models in Table 1. The corresponding solution to each model is presented in Figure 8. The AICc is calculated as $AIC_c = n\ln\left(\frac{SSE}{n}\right) + 2k + \frac{2k(k+1)}{n-k-1}$. The smallest AICc value is bolded.

4.1.6 Dataset 6

Fitting the six models in Table 1 to B16-F10 tumor growth data in NSG mice provided in dataset 6 [18] lead to the Von Bertalanffy 2 model being the best fit, with the smallest AICc value of -23.1835, followed by the Logistic model, with an AICc of -21.9501 (See Table 13). Moreover, for dataset 6, the Logistic model and Gompertz 1 and 2 models are considered to be equivalent to the best fit as the difference between their AICc value and the minimum AICc value is $\leq$ to 4. We estimated the growth parameters for the Von Bertalanffy 2 model to be $\alpha = -2.6600 \times 10^{-2}\ h^{-1}$ and $\beta = -2.1784 \times 10^{1}\ cells^{-1}$. The resulting parameter estimates and AICc values for the six growth models are reported in Table 13. The model best fit model solutions are plotted along with the data in Figure 9.

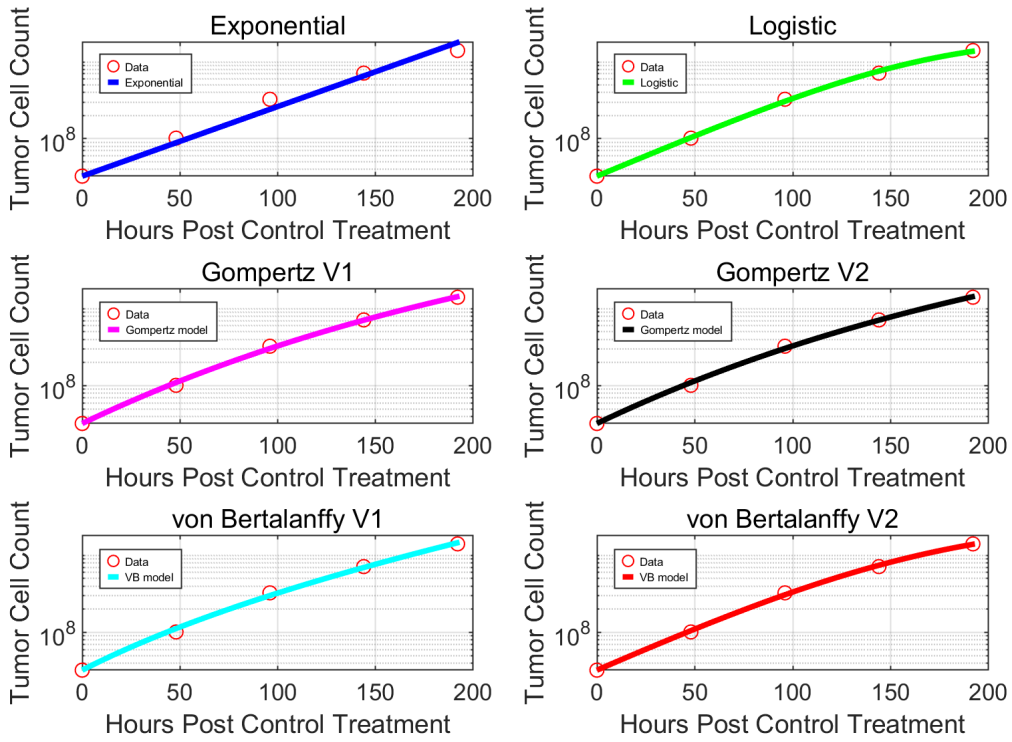


Figure 9: Data fitting results (Dataset 6): Datapoints from day 9 to 17 (red circles) [18] are fit to the tumor growth (solid lines) models listed in Table 1. Best fit parameters for each model is given in Table 13.

(Model)	Equation	(Parameters)	fval (SSE)	k	AICc
Logistic	$\frac{dT}{dt} = rT\left(1 - \frac{T}{K}\right)$	$r = 2.4837 \times 10^{-2}\ h^{-1}$ $K = 2.1306 \times 10^{9} cells$	8.3911×10^{-3}	2	-21.9501
Exponential	$\frac{dT}{dt} = rT$	$r = 2.0875 \times 10^{-2}\ h^{-1}$	1.7489×10^{-1}	1	-13.4319
Gompertz 1	$\frac{dT}{dt} = G_0 e^{-\alpha t} T$	$G_0 = 2.7871 \times 10^{-2}\ h^{-1}$ $\alpha = 3.8421 \times 10^{-3}\ h^{-1}$	1.1718×10^{-2}	2	-20.2804
Gompertz 2	$\frac{dT}{dt} = aT\ln\left(\frac{1}{bT}\right)$	$a = 3.8593 \times 10^{-3}\ h^{-1}$ $b = -2.4529 \times 10^{1}\ cells^{-1}$	1.1712×10^{-2}	2	-20.2830
Von Bertalanffy 1	$\frac{dT}{dt} = \alpha T^{2/3} - \beta T$	$\alpha = 6.7736 \times 10^{0}\ cells^{\frac{1}{3}} h^{-1}$ $\beta = -8.6326 \times 10^{-3}\ h^{-1}$	1.8403×10^{-2}	2	-18.0234
Von Bertalanffy 2	$\frac{dT}{dt} = \alpha T((\beta T)^{2/3} - 1)$	$\alpha = -2.6600 \times 10^{-2}\ h^{-1}$ $\beta = -2.1784 \times 10^{1}\ cells^{-1}$	6.5567×10^{-3}	2	**-23.1835**

Table 13: Comparison between six tumor growth models (Dataset 6) [18]. The corresponding solution to each model is presented in Figure 9. The AICc is calculated as $AIC_c = n\ln\left(\frac{SSE}{n}\right) + 2k + \frac{2k(k+1)}{n-k-1}$. The smallest AICc value is bolded.

4.1.7 Summary of results

The fitting results across multiple datasets demonstrated that the **Von Bertalanffy I (VB 1)** model consistently exhibited superior or equivalent performance, as determined by having smallest or relatively

small AICc values across all 6 datasets. Specifically, VB I was the best fit for Datasets 1 and 5. In Dataset 4, Gompertz I and VB I showed equivalent performance because the difference between their AICc values is smaller than 4. For Dataset 3, all candidate models fit the data equally well. Datasets 2 and 6 did not allow the tumors to reach saturation due to shorter experimental durations, making it impossible to effectively differentiate model performance. In these cases, exponential and VB 2 model was the best fit. These datasets have only five datapoints each, which means the tumor cell population is not given long enough time to saturate. This possibly explains why VB 1 model does not fit well.

Biologically, the Von Bertalanffy I model suggests that melanoma growth is governed by a dynamic balance between proliferative activity and resource limitations (such as nutrients and space) within the tumor microenvironment. This realistic framework makes it highly suitable for studying tumor–immune interactions in subsequent research.

Item	**[12] (DS 1)**	**[14] (DS 2)**	**[15] (DS 3)**	**[16] (DS 4)**	**[17] (DS 5)**	**[18] (DS 6)**
Tumor	B16-F10	B16-F10	B16-F10	B16-F10	B16/F10-OVA	B16-F10
Mice immune deficiency	NOD-SCID	NOD-SCID*	SCID	SCID	NOD-SCID	NSG
Age (week)	8-12	6-8	10-12	/	6	8
Sex	Male	Female	Female	/	Male	/
Control drug	Saline	PBS	/	/	PBS	Vehicle**
Experiment length (day)	10	8	6	12	14	8
Best Fit Model	VB 1	Exp	Exp	G1	VB 1	VB 2
Equivalent Best*** Models	/	log	all	VB1	/	log,G1,G2

* addition: NOD-SCID*/IL-2gR knockout
** Vehicle: methylcellulose (0.5% in water) supplemented with 1% polysorbate 80.
*** Equivalence: $AICc_i - AICc_{min} \leq 4$

Table 14: Summary of experiments used for fitting tumor growth models given in Table 1 and summary of model selection outcomes.

5 Stability Analysis: Model 1

We analyze the three-compartment tumor-immune system without PKM2 treatment:

$$\frac{dT}{dt} = \alpha T^{2/3} - \beta T - \delta_E \frac{(E/T)}{s + (E/T)} T - \delta_F \frac{T}{h_{T,F} + T} F, \tag{24a}$$

$$\frac{dE}{dt} = \frac{T}{h_{E,T} + T} E(p_E + \sigma_F F) - c_T T E - \mu_E E, \tag{24b}$$

$$\frac{dF}{dt} = p_F \frac{T}{h_{F,T} + T} E - \mu_F F. \tag{24c}$$

All parameters $\alpha, \beta, \delta_E, \delta_F, s, h_{T,F}, h_{E,T}.h_{F,T}, p_E, p_F, \sigma_F, c_T, \mu_E, \mu_F$ are assumed strictly positive and we let the exponent $\lambda = 1$ so that the effector-mediated killing term reduces to a standard Michaelis-Menten form, to preserve the saturating nature of the killing response while allowing the coexistence equilibria to be reduced to the roots of a single polynomial equation.

Equilibria (T^*, E^*, F^*) are found by substituting $T^*, E^*,$ and F^* into the system (24a)-(24c) for $T, E,$ and F, respectively, setting the right-hand sides of (24a)-(24c) to zero and solving for $T^*, E^*,$ and F^* simultaneously. The system admits three biologically named equilibria: a tumor free state, a tumor-only state, and one or more coexistence states.

Proposition 1. *The point $(T^*, E^*, F^*) = (0, 0, 0)$ is the only unique tumor-free equilibrium of (24), and it is unstable for every choice of positive parameters.*

Proof. Existence: At $T = 0$, (24b) and (24c) are reduced down to $\dot{E} = -\mu_E E$ and $\dot{F} = -\mu_F F$, meaning the rate of change can only be 0 if $E = F = 0$. If we substitute that back into (24a), that vanishes as well. Unlike most models with a constant immune source independent of T, [8], here the proliferation of E and F is strictly dependent on their encounter with tumor antigens, so no non-zero tumor-free immune equilibrium can exist.
Stability: The term $T^{2/3}$ is not differentiable at $T = 0$, so the Jacobian of (24) is undefined at the $(0, 0, 0)$ state. Following Ajbar et al. [9], who establish the analogous result for a two-compartment von-Bertalanffy tumor-immune model, the tumor-free equilibrium is unstable for all positive parameter values. The instability arises precisely because of this non-differentiability of $T^{2/3}$ at the origin: near T=0, the tumor's intrinsic growth term dominates the immune mediated loss terms, regardless of parameter values. □

Proposition 2. *The point* $\left(T^*, E^*, F^*\right) = \left(\left(\frac{\alpha}{\beta}\right)^3, 0, 0\right)$ *is an equilibrium of* (24)*, and it is asymptotically stable if and only if*

$$\frac{T^*}{h_{E,T} + T^*} p_E \;<\; c_T T^* + \mu_E, \qquad T^* = \left(\frac{\alpha}{\beta}\right)^3. \tag{25}$$

Proof. Existence: setting $E = F = 0$ collapses (24a) to $\dot{T} = \alpha T^{2/3} - \beta T = T^{2/3}(\alpha - \beta T^{1/3})$, which vanishes at $T = 0$ and at $T^* = (\alpha/\beta)^3$. This represents the tumor's intrinsic carrying capacity-type equilibrium in the complete absence of an immune response.
Stability: Since $\dot{E}$ and $\dot{F}$ are each proportional to E, the Jacobian at $(T^*, 0, 0)$ is lower block-triangular:

$$J\big|_{(T^*,0,0)} = \begin{pmatrix} \frac{2}{3}\alpha T^{*-1/3} - \beta & -\frac{\delta_E}{s} & -\frac{\delta_F T}{h_{T,F}+T^*} \\ 0 & \dfrac{T^*}{h_{E,T}+T^*} p_E - c_T T^* - \mu_E & 0 \\ 0 & \dfrac{T^*}{h_{F,T}+T^*} p_F & -\mu_F \end{pmatrix}. \tag{26}$$

Using $\alpha = \beta T^{*1/3}$, the J_{11} entry simplifies to $\frac{2}{3}\beta - \beta = -\frac{1}{3}\beta < 0$ always, and the J_{33} entry is $-\mu_F < 0$ always. The three eigenvalues are the diagonal entries; only the middle one,

$$\lambda_E = \frac{T^*}{h_{E,T} + T^*} p_E - c_T T^* - \mu_E, \tag{27}$$

has parameter dependent sign giving stability condition (25). □

Looking at the left side of (25) we see the effector proliferation rate that is induced by tumor presence; the right side is the sum of tumor-induced effector inactivation and natural effector death. When proliferation rate cannot keep up with the loss, the immune presence collapses at the tumor-only state which becomes a locally asymptotically stable equilibrium corresponding to unchecked tumor growth despite an initially engaged immune response. When the inequality is reversed, this state is unstable, allowing the immune response to invade.

5.1 Coexistence Equilibria

Coexistence equilibria $(\hat{T}, \hat{E}, \hat{F})$, with all three components strictly positive, are obtained by eliminating E and F from the full system and reducing to a single polynomial equation.

Assuming $E \neq 0$, every term of (24b) carries a common factor of E; dividing by E and setting the result to zero gives

$$\frac{T}{h_{E,T} + T}(p_E + \sigma_F F) - c_T T - \mu_E = 0, \tag{28}$$

which is linear in F and solves explicitly as

$$F(T) = \frac{Q(T)}{T\sigma_F}, \qquad Q(T) := (c_T T + \mu_E)(h_{E,T} + T) - p_E T. \tag{29}$$

Substituting (29) into the steady-state form of (24c), $p_F \frac{T}{h_{F,T}+T} E = \mu_F F$, and solving for E yields

$$E(T) = \frac{\mu_F(h_{F,T}+T)}{p_F T} F(T) = \frac{\mu_F(h_{F,T}+T)\,Q(T)}{p_F \sigma_F\, T^2}. \tag{30}$$

Both $E(T)$ and $F(T)$ become explicit functions of T. $Q(T) = c_T T^2 + (c_T h_{E,T} + \mu_E - p_E)T + \mu_E h_{E,T}$, and notice when $Q(T^*)$ is evaluated at the tumor only equilibrium $T^* = (\alpha/\beta)^3$ is exactly the negative of the stability condition (25), ie, $Q(T^*) > 0$ if and only if $(T^*, 0, 0)$ is stable.
Substituting (30) and (29) into the steady state form ot (24a), and multiplying through by all remaining denominators, and applying the substitution $T = u^3$ gives us a polynomial equation.

$$F(u) = A_0 + A_2u^2 + A_3u^3 + A_5u^5 + A_6u^6 + A_8u^8 + A_9u^9 + A_{11}u^{11} + A_{12}u^{12} + A_{14}u^{14} + A_{15}u^{15} = 0. \tag{31}$$

Such that the coefficients are as follows:

$$\begin{aligned}
A_0 &= -\delta_F h_{E,T}^2 h_{F,T} \mu_E^2 \mu_F,\\
A_2 &= \alpha h_{E,T} h_{F,T} h_{T,F} \mu_E \mu_F \sigma_F,\\
A_3 &= -h_{E,T}\mu_E\mu_F\Big[2c_T\delta_F h_{E,T} h_{F,T} + \delta_F\big(h_{E,T}\mu_E + 2h_{F,T}(\mu_E - p_E)\big) + B h_{F,T} h_{T,F}\sigma_F\Big],\\
A_5 &= \alpha\mu_F\sigma_F\Big[c_T h_{E,T} h_{F,T} h_{T,F} + h_{E,T}H_2\mu_E + h_{F,T}h_{T,F}(\mu_E - p_E)\Big],\\
A_6 &= -\mu_F\Big[C_2 h_{E,T}^2 h_{F,T} + \delta_F\big(2h_{E,T}\mu_E + h_{F,T}(\mu_E - p_E)\big)(\mu_E - p_E) + B\big(h_{E,T}H_2\mu_E + h_{F,T}h_{T,F}(\mu_E - p_E)\big)\sigma_F + c_T h_{E,T}\Big(2\delta_F\big(h_{E,T}\mu_E + 2h_{F,T}\mu_E - h_{F,T}p_E\big) + B h_{F,T}h_{T,F}\sigma_F\Big)\Big],\\
A_8 &= \alpha\mu_F\sigma_F\Big[c_T h_{F,T}h_{T,F} + c_T h_{E,T}H_2 + h_{E,T}\mu_E + H_2(\mu_E - p_E)\Big],\\
A_9 &= -C_2 h_{E,T}(h_{E,T} + 2h_{F,T})\mu_F - B\mu_F\Big[h_{E,T}\mu_E + H_2(\mu_E - p_E)\Big]\sigma_F - c_T\mu_F\Big[2\delta_F\big(2h_{E,T}\mu_E + h_{F,T}\mu_E - h_{E,T}p_E - h_{F,T}p_E\big) + B\big(h_{F,T}h_{T,F} + h_{E,T}H_2\big)\sigma_F\Big] - \delta_F\Big[\mu_F(\mu_E - p_E)^2 + h_{E,T}\mu_E K\sigma_F\Big],\\
A_{11} &= \alpha\sigma_F\Big[c_T H_3\mu_F + \mu_F(\mu_E - p_E) + h_{T,F}K\sigma_F\Big],\\
A_{12} &= -C_2(2h_{E,T} + h_{F,T})\mu_F - c_T\Big[B H_3\mu_F\sigma_F + \delta_F\big(2\mu_F(\mu_E - p_E) + h_{E,T}K\sigma_F\big)\Big] - \sigma_F\Big[(\mu_E - p_E)(\delta_E\mu_F + \delta_F K) + \beta\big(\mu_F(\mu_E - p_E) + h_{T,F}K\sigma_F\big)\Big],\\
A_{14} &= \alpha\sigma_F\big(c_T\mu_F + K\sigma_F\big).\\
A_{15} &= -\Big[C_2\mu_F + c_T\big(\beta\mu_F + \delta_E\mu_F + \delta_F K\big)\sigma_F + \beta K\sigma_F^2\Big].
\end{aligned}$$

(where $B := \beta + \delta_E$, $H_2 := h_{F,T} + h_{T,F}$, $H_3 := h_{E,T} + h_{F,T} + h_{T,F}$, $K := p_F s$, and $C_2 := c_T^2\delta_F$ collect recurring combinations of parameters appearing throughout the coefficients above.)

$F(u)$ is a polynomial of degree 15 with 11 nonzero coefficients, at powers $u^0, u^2, u^3, u^5, u^6, u^8, u^9, u^{11}, u^{12}, u^{14}, u^{15}$. Every coexistence equilibrium of the model corresponds to a positive real root u^* of (31) satisfying the additional validity conditions $E(u^{*3}) \geq 0$ and $F(u^{*3}) \geq 0$, evaluated from Equations (29)-(30); the corresponding tumor level is $\hat{T} = (u^*)^3$. Since $Q(T)$ is a quadratic with positive leading coefficient c_T and positive constant term $\mu_E h_{E,T}$, it has either zero or two real roots, and $F(T)$, $E(T)$ therefore each change sign at most twice on $T > 0$; this restricts which roots of Equation (31) can correspond to biologically valid equilibria. This procedure directly follows the elimination strategy used by Yu et al. [35] which they used for a five-compartment oncolytic virotherapy model and by [9] for their two compartment tumor-immune model.

Table 15 classifies each nonzero coefficient by whether its sign is determined by the positivity of the parameters alone and not the value. We notice that every indeterminate coefficient's sign ambiguity can be traced back to a single recurring quantity $(\mu_E - p_E)$ which is the effector death rate vs effector proliferation rate. We see the same comparison in the tumor-only stability condition (25). Following Ajbar et al. [9], the fixed-sign coefficients alone $(-, +, ..., +, -)$ guarantee at least two sign changes, so Descartes' rule of signs gives us a lower bound of at least 2 and an upper bound of 11 possible positive real roots of (31). The exact count depends on the indeterminate coefficients and, in general, requires numerical evaluation once parameter values are specified.

Power of u	Sign
u^0	Always negative
u^2	Always positive
u^3	Indeterminate
u^5	Indeterminate
u^6	Indeterminate
u^8	Indeterminate
u^9	Indeterminate
u^{11}	Indeterminate
u^{12}	Indeterminate
u^{14}	Always positive
u^{15}	Always negative

Table 15: Sign classification of the coefficients of the degree-15 polynomial $F(u)$ in Equation (31).

Proposition 3. *Let $u^* = \alpha/\beta$ (the location of the tumor-only equilibrium in the u-coordinate). Then $F(u^*)$ factors as*

$$F(u^*) = -\frac{1}{\beta^{15}}\left[(T^* + h_{E,T})(c_T T^* + \mu_E) - p_E T^*\right] \times G(\alpha, \beta, \ldots), \tag{32}$$

where $T^* = (\alpha/\beta)^3$ and G is a second, generally sign-indeterminate expression in the model parameters. In particular, the bracketed factor is exactly the negative of the left-minus-right side of the master stability condition (25).

This was verified by direct substitution and simplification of (31) at $u = u^*$ through Mathematica. It provides a cross check between the coexistence-equilibrium polynomial (derived via nullcline elimination) and the tumor-only stability condition (derived via Jacobian evaluation), the two calculations that were performed by two different methods agree exactly. This mirrors the result of Yu et al. [35] who show for their cubic $g(x)$ that $g(K) > 0$ is algebraically equivalent to the stability condition of their boundary equilibrium $(K, 0, 0)$. Unlike their case, however, $F(u^*)$ here factors as a product of two expressions rather than reducing to the stability condition alone, which just reflects the algebraic complexity that was added by having a saturating kill term rather than a mass action kill term and the additional cytokine compartment.

Equilibrium	Location	Stability
Tumor-free	$(0, 0, 0)$	Unstable for all positive parameters
Tumor-only	$\left((\alpha/\beta)^3, 0, 0\right)$	Stable iff (25) holds
Coexistence	$\left(\bar{T}, \bar{E}, \bar{F}\right)^*$	Determined by Jacobian at each steady state

* Where $\bar{T}$ are the positive roots of Equation (31) and $\bar{E}$ and $\bar{F}$ are determined by $E(\bar{T})$ and $F(\bar{T})$ given in Equation (30) and Equation (29), respectively.

Table 16: Summary of steady state and stability of equilibria in Model 1 given in Equation (24).

5.2 Summary

The unconditional instability of the tumor-free equilibrium (Proposition 1) implies that, in this model, complete tumor elimination cannot occur as an asymptotically stable outcome for any choice of parameters; the best attainable long-term outcome is convergence to a coexistence equilibrium with small tumor burden, when one exists and is stable, rather than a true cure. This is a structural consequence of the von Bertalanffy growth law and is consistent with the analogous finding of Ajbar et al [9] for their two compartment reduction.

6 Discussion and Future Work

The results of this study support the use of the von Bertalanffy growth law as a biologically realistic and mathematically tractable foundation for tumor-immune modeling. Fitting to six independent B16-F10 melanoma datasets showed that the von Bertalanffy model consistently matched or outperformed the exponential, logistic, and Gompertz alternatives, justifying its use throughout Models 1-3.

This growth law also carries a direct analytical consequence: the tumor-free equilibrium is unconditionally unstable, for any choice of immune parameters, because the term $T^{2/3}$ dominates all bounded immune-killing terms near $T = 0$. As a result, complete tumor elimination cannot arise as a stable outcome of the reduced model; the best attainable outcome is a stable coexistence equilibrium with small tumor burden. This mirrors the analogous finding of Ajbar et al. [9] for a two-compartment von Bertalanffy model and stands in contrast to logistic-growth frameworks, where the tumor-free state's stability depends on parameter values.

The stability of the tumor-only equilibrium was shown to depend on a single inequality comparing tumor-driven effector proliferation against the combined rate of exhaustion and natural effector death. This condition involves precisely the quantities that PKM2 activation is reported to affect proliferation and exhaustion, suggesting a direct mathematical link between the treatment's known biological effects and its predicted capacity to destabilize uncontrolled tumor growth in this framework.

Finally, the coexistence equilibria were shown to correspond to the positive real roots of a degree-15 polynomial, extending the reduction strategies used in comparable models [9, 35]. A recurring sign ambiguity across several polynomial coefficients traced back to the same quantity governing the tumor-only stability condition, and this connection was confirmed directly by an exact factorization of the polynomial at the tumor-only equilibrium's location.

These results are limited to the untreated, reduced form of Model 1. Extending the equilibrium analysis to the full treatment model, and to the memory-subset extensions in Models 2 and 3, remains an important direction for future work, along with a numerical bifurcation analysis using PKM2 activation as the bifurcation parameter. A further direction for future work is quantitative validation of the models against experimental data. Current steady states and coefficients are analytical and hold for arbitrary positive parameter values. The next step would be to fit the model's immune response parameters as well as the multi-scale model's parameters to the TEPP46 treatment data reported in Farsani et al. [7].

7 Appendix

7.1 Parameter Estimation

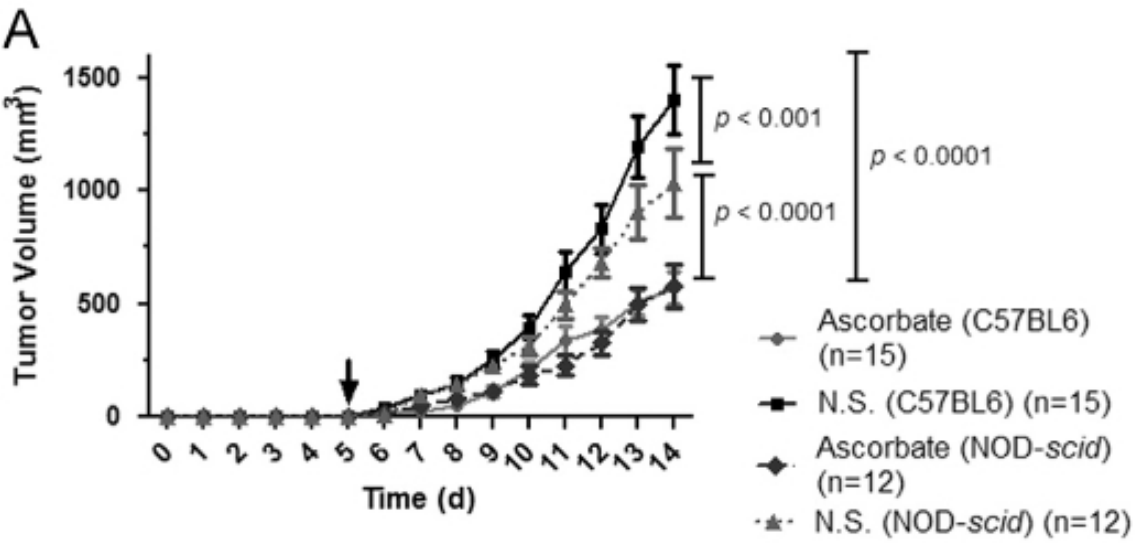


Figure 10: Data from dataset 1 [12].

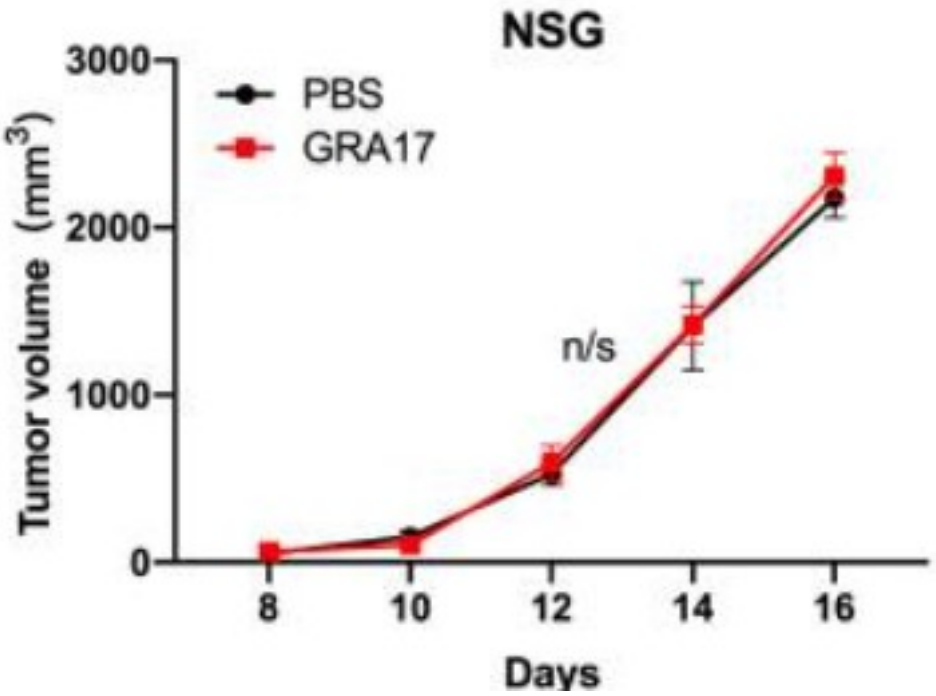


Figure 11: Data from dataset 2 [14].

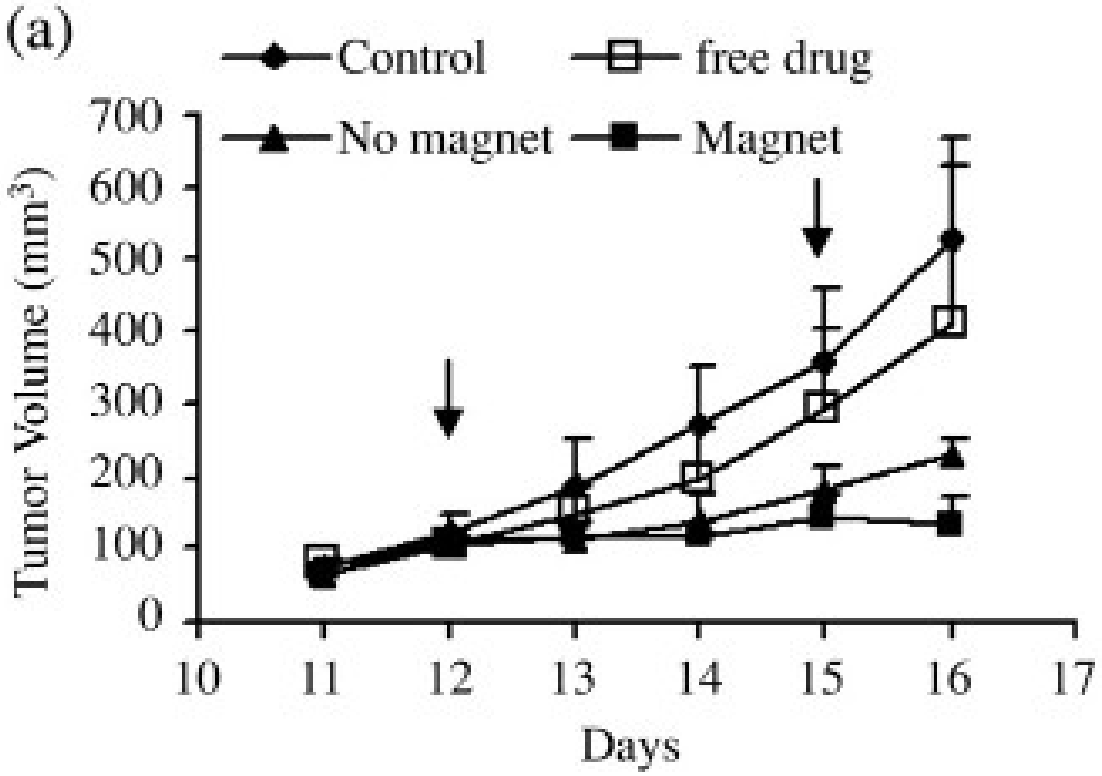


Figure 12: Data from dataset 3 [15].

Figure 8

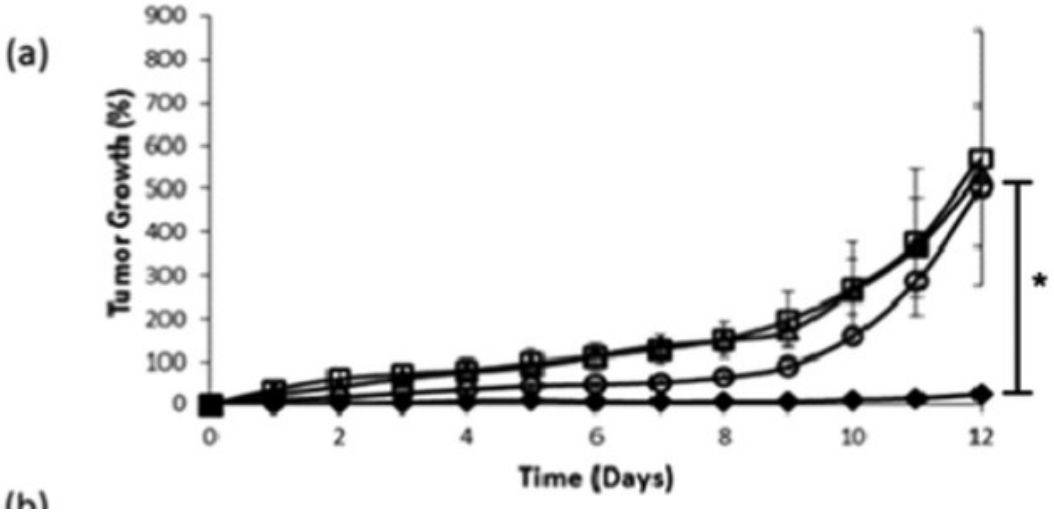


Figure 13: Data from dataset 4 [16].

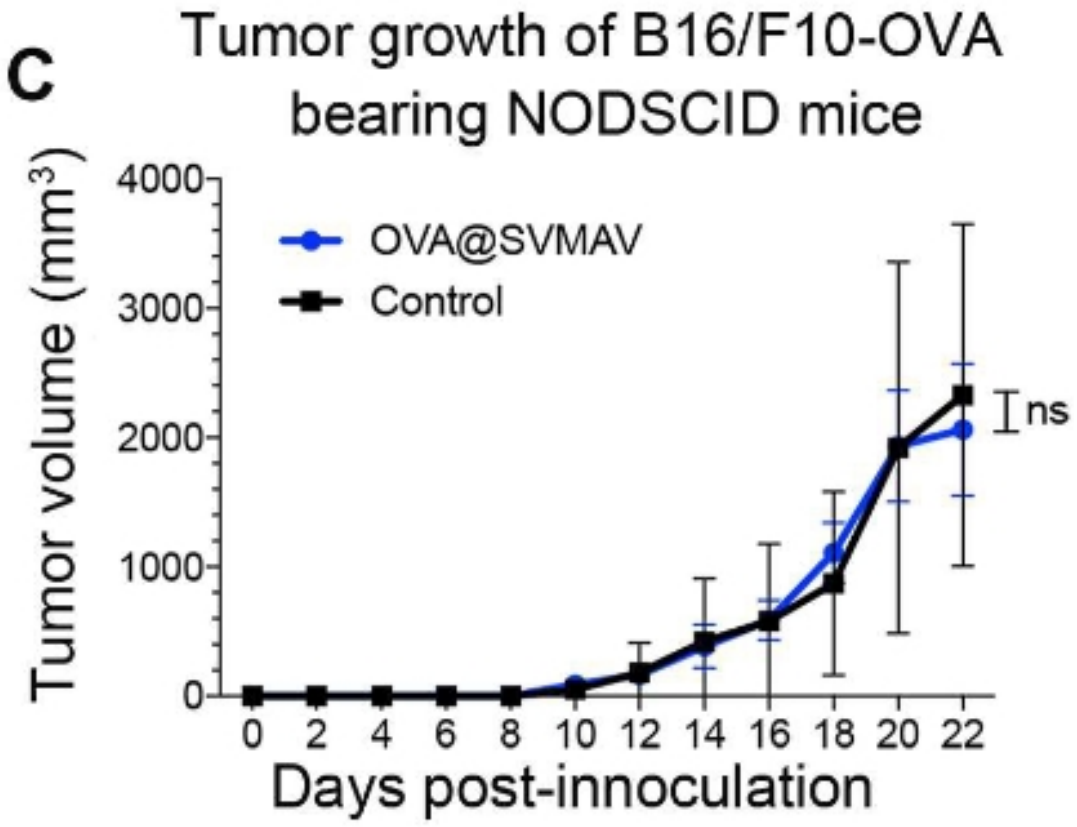


Figure 14: Data from dataset 5 [17].

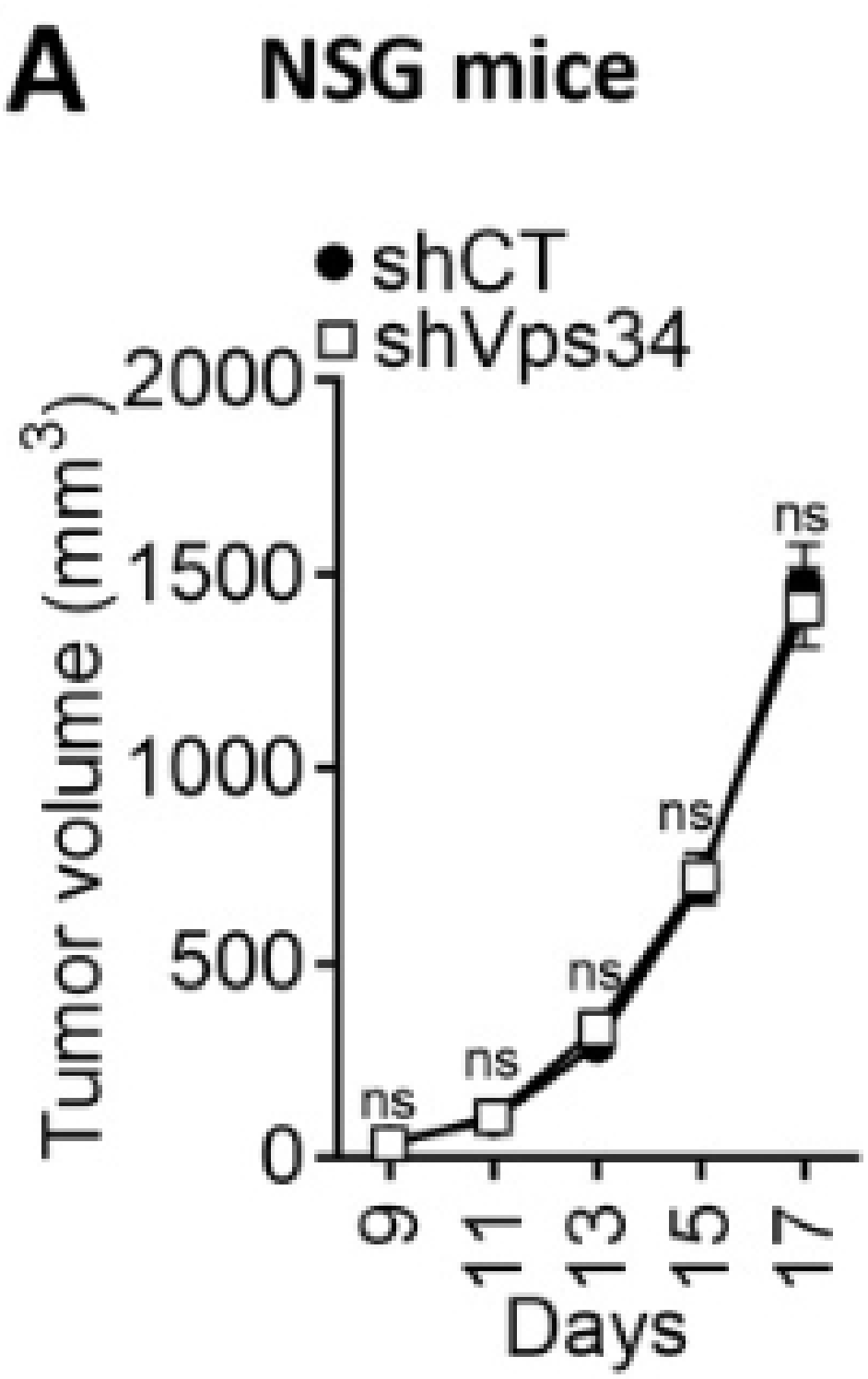


Figure 15: Data from dataset 6 [18].

References

[1] Sibaji Sarkar, Garrick Horn, Kimberly Moulton, Anuja Oza, Shannon Byler, Shannon Kokolus, and McKenna Longacre. Cancer development, progression, and therapy: an epigenetic overview. *International journal of molecular sciences*, 14(10):21087–21113, 2013. doi: 10.3390/ijms141021087. URL https://doi.org/10.3390/ijms141021087.

[2] Lynda Wyld, Riccardo A Audisio, and Graeme J Poston. The evolution of cancer surgery and future perspectives. *Nature Reviews Clinical Oncology*, 12(2):115–124, 2015. doi: 10.1038/nrclinonc.2014.191. URL https://doi.org/10.1038/nrclinonc.2014.191.

[3] Elizabeth V Maani and Christopher V Maani. Radiation therapy. In *StatPearls [Internet]*. StatPearls Publishing, Treasure Island (FL), October 2022. URL https://www.ncbi.nlm.nih.gov/books/NBK537036/. [Updated 2022 Oct 24].

[4] Muhammad T Amjad, Anusha Chidharla, and Anup Kasi. Cancer chemotherapy. In *StatPearls [Internet]*. StatPearls Publishing, Treasure Island (FL), February 2023. URL https://www.ncbi.nlm.nih.gov/books/NBK564367/. [Updated 2023 Feb 27].

[5] Valencia McNeil and Seung Won Lee. Advancing cancer treatment: A review of immune checkpoint inhibitors and combination strategies. *Cancers*, 17(9):1408, 2025. doi: 10.3390/cancers17091408. URL https://doi.org/10.3390/cancers17091408.

[6] Peter Vaupel, Heinz Schmidberger, and Arnulf Mayer. The warburg effect: essential part of metabolic reprogramming and central contributor to cancer progression. *International journal of radiation biology*, 95(7):912–919, 2019. doi: 10.1080/09553002.2019.1589653. URL https://doi.org/10.1080/09553002.2019.1589653.

[7] Seyedeh Sahar Mortazavi Farsani, Jignesh Soni, Lu Jin, Anil Kumar Yadav, Shivani Bansal, Tian Mi, Leena Hilakivi-Clarke, Robert Clarke, Benjamin Youngblood, Amrita Cheema, et al. Pyruvate kinase m2 activation reprograms mitochondria in cd8 t cells, enhancing effector functions and efficacy of anti-pd1 therapy. *Cell Metabolism*, 37(6):1294–1310, 2025. URL https://doi.org/10.1016/j.cmet.2025.03.003.

[8] Lisette G. de Pillis and Ami E. Radunskaya. Modeling tumor–immune dynamics. In Amina Eladdadi, Peter Kim, and Dann Mallet, editors, *Mathematical Models of Tumor-Immune System Dynamics*, pages 59–108, New York, NY, 2014. Springer New York. ISBN 978-1-4939-1793-8. doi: 10.1007/978-1-4939-1793-8_3. URL https://doi.org/10.1007/978-1-4939-1793-8_3.

[9] Abdelhamid Ajbar, Rubayyi T Alqahtani, and Khalid Alhumaizi. Bifurcation study of a tumor-immune system with chemotherapy. *PLoS One*, 20(7):e0327304, 2025.

[10] Jui-Ling Yu, Sophia R-J Jang, and Kwei-Yan Liu. Exploring the interactions of oncolytic viral therapy and immunotherapy of anti-ctla-4 for malignant melanoma mice model. *Cells*, 12(3):507, 2023. doi: 10.3390/cells12030507. URL https://doi.org/10.3390/cells12030507.

[11] Joseph E Cavanaugh and Andrew A Neath. The akaike information criterion: Background, derivation, properties, application, interpretation, and refinements. *Wiley Interdisciplinary Reviews: Computational Statistics*, 11(3):e1460, 2019. doi: 10.1002/wics.1460. URL https://doi.org/10.1002/wics.1460.

[12] Oscar K Serrano, Nermi L Parrow, Pierre-Christian Violet, Jacqueline Yang, Jennifer Zornjak, Agnes Basseville, and Mark Levine. Antitumor effect of pharmacologic ascorbate in the b16 murine melanoma model. *Free Radical Biology and Medicine*, 87:193–203, 2015. doi: 10.1016/j.freeradbiomed.2015.06.032. URL https://doi.org/10.1016/j.freeradbiomed.2015.06.032.

[13] Ankit Rohatgi. Webplotdigitizer, 2024. URL https://automeris.io/WebPlotDigitizer. Version 4.7.

[14] Yu-Chao Zhu, Hany M Elsheikha, Jian-Hua Wang, Shuai Fang, Jun-Jun He, Xing-Quan Zhu, and Jia Chen. Synergy between toxoplasma gondii type i δgra17 immunotherapy and pd-l1 checkpoint inhibition triggers the regression of targeted and distal tumors. *Journal for immunotherapy of cancer*, 9(11): e002970, 2021. doi: 10.1136/jitc-2021-002970. URL https://doi.org/10.1136/jitc-2021-002970.

[15] Suman Dandamudi, Vishwesh Patil, William Fowle, Ban-An Khaw, and Robert B Campbell. External magnet improves antitumor effect of vinblastine and the suppression of metastasis. *Cancer science*, 100(8):1537–1543, 2009. doi: 10.1111/j.1349-7006.2009.01201.x. URL https://doi.org/10.1111/j.1349-7006.2009.01201.x.

[16] Simanpreet Kaur Dhillon, Simon L Porter, Nermeen Rizk, Yingjie Sheng, Thomas McKaig, Kathyrn Burnett, Bronagh White, Heather Nesbitt, Rubeta N Matin, Anthony P McHale, et al. Rose bengal–amphiphilic peptide conjugate for enhanced photodynamic therapy of malignant melanoma. *Journal of Medicinal Chemistry*, 63(3):1328–1336, 2020. doi: 10.1021/acs.jmedchem.9b01802. URL https://pubs.acs.org/doi/10.1021/acs.jmedchem.9b01802.

[17] Lele Zhang, Jiacheng Huang, Xiaona Chen, Caixu Pan, Yong He, Rong Su, Danjing Guo, Shengyong Yin, Shuai Wang, Lin Zhou, et al. Self-assembly nanovaccine containing tlr7/8 agonist and stat3 inhibitor enhances tumor immunotherapy by augmenting tumor-specific immune response. *Journal for Immunotherapy of Cancer*, 9(8):e003132, 2021. doi: 10.1136/jitc-2021-003132. URL https://doi.org/10.1136/jitc-2021-003132.

[18] Muhammad Zaeem Noman, Santiago Parpal, Kris Van Moer, Malina Xiao, Yasmin Yu, Tsolere Arakelian, Jenny Viklund, Angelo De Milito, Meriem Hasmim, Martin Andersson, et al. Inhibition of vps34 reprograms cold into hot inflamed tumors and improves anti–pd-1/pd-l1 immunotherapy. *Science advances*, 6(18):eaax7881, 2020. doi: 10.1126/sciadv.aax7881. URL https://doi.org/10.1126/sciadv.aax7881.

[19] Jichang Han, Nikhil Khatwani, Tyler G Searles, Mary Jo Turk, and Christina V Angeles. Memory cd8+ t cell responses to cancer. In *Seminars in immunology*, volume 49, page 101435. Elsevier, 2020. doi: 10.1016/j.smim.2020.101435. URL https://doi.org/10.1016/j.smim.2020.101435.

[20] F Crauste, J Mafille, L Boucinha, S Djebali, O Gandrillon, J Marvel, et al. Identification of nascent memory cd8 t cells and modeling of their ontogeny, cell syst., 4 (2017), 306–317. URL https://doi.org/10.1016/j.cels.2017.01.014.

[21] Itziar Frades, Carles Foguet, Marta Cascante, and Marcos J Araúzo-Bravo. Genome scale modeling to study the metabolic competition between cells in the tumor microenvironment. *Cancers*, 13(18):4609, 2021. doi: 10.3390/cancers13184609. URL https://doi.org/10.3390/cancers13184609.

[22] Veronika I Zarnitsyna, Andreas Handel, Sean R McMaster, Sarah L Hayward, Jacob E Kohlmeier, and Rustom Antia. Mathematical model reveals the role of memory cd8 t cell populations in recall responses to influenza. *Frontiers in immunology*, 7:165, 2016. doi: 10.3389/fimmu.2016.00165. URL https://doi.org/10.3389/fimmu.2016.00165.

[23] Cicely Macnamara and Raluca Eftimie. Memory versus effector immune responses in oncolytic virotherapies. *Journal of theoretical biology*, 377:1–9, 2015. URL https://doi.org/10.1016/j.jtbi.2015.04.004.

[24] Derek C Macallan, José AM Borghans, and Becca Asquith. Human t cell memory: A dynamic view. *Vaccines*, 5(1):5, 2017. doi: 10.3390/vaccines5010005. URL https://doi.org/10.3390/vaccines5010005.

[25] Nikhil S Joshi, Weiguo Cui, Anmol Chandele, Heung Kyu Lee, David R Urso, James Hagman, Laurent Gapin, and Susan M Kaech. Inflammation directs memory precursor and short-lived effector cd8+ t cell fates via the graded expression of t-bet transcription factor. *Immunity*, 27(2):281–295, 2007. doi: 10.1016/j.immuni.2007.07.010. URL https://doi.org/10.1016/j.immuni.2007.07.010.

[26] Susan M Kaech and E John Wherry. Heterogeneity and cell-fate decisions in effector and memory cd8+ t cell differentiation during viral infection. *Immunity*, 27(3):393–405, 2007. doi: 10.1016/j.immuni.2007.08.007. URL https://doi.org/10.1016/j.immuni.2007.08.007.

[27] M Jeon, HW Kang, and S An. A mathematical model for enzyme clustering in glucose metabolism. sci rep. 2018; 8: 2696, 2018. URL https://www.nature.com/articles/s41598-018-20348-7.

[28] Berta Mendoza-Juez, Alicia Martínez-González, Gabriel F Calvo, and Víctor M Pérez-García. A mathematical model for the glucose-lactate metabolism of in vitro cancer cells. *Bulletin of mathematical biology*, 74(5):1125–1142, 2012. URL https://doi.org/10.1007/s11538-011-9711-z.

[29] Jiansheng Xie, Hao Wu, Chunyan Dai, Qiangrong Pan, Zonghui Ding, Danqing Hu, Bingyan Ji, Yan Luo, and Xun Hu. Beyond warburg effect–dual metabolic nature of cancer cells. *Scientific reports*, 4 (1):4927, 2014. doi: 10.1038/srep04927. URL https://doi.org/10.1038/srep04927.

[30] Irina Kareva and Faina Berezovskaya. Cancer immunoediting: a process driven by metabolic competition as a predator–prey–shared resource type model. *Journal of theoretical biology*, 380:463–472, 2015. URL https://doi.org/10.1016/j.jtbi.2015.06.007.

[31] Madhusudhanan Sukumar, Jie Liu, Yun Ji, Murugan Subramanian, Joseph G Crompton, Zhiya Yu, Rahul Roychoudhuri, Douglas C Palmer, Pawel Muranski, Edward D Karoly, et al. Inhibiting glycolytic metabolism enhances cd8+ t cell memory and antitumor function. *The Journal of clinical investigation*, 123(10):4479–4488, 2013. doi: 10.1172/JCI69589. URL https://doi.org/10.1172/JCI69589.

[32] Patrick M Gubser, Glenn R Bantug, Leyla Razik, Marco Fischer, Sarah Dimeloe, Gideon Hoenger, Bojana Durovic, Annaïse Jauch, and Christoph Hess. Rapid effector function of memory cd8+ t cells requires an immediate-early glycolytic switch. *Nature immunology*, 14(10):1064–1072, 2013. doi: 10.1038/ni.2687. URL https://doi.org/10.1038/ni.2687.

[33] Jessica B McGillen, Catherine J Kelly, Alicia Martínez-González, Natasha K Martin, Eamonn A Gaffney, Philip K Maini, and Víctor M Pérez-García. Glucose–lactate metabolic cooperation in cancer: Insights from a spatial mathematical model and implications for targeted therapy. *Journal of theoretical biology*, 361:190–203, 2014. URL https://doi.org/10.1016/j.jtbi.2014.09.018.

[34] Kévin Spinicci, Pierre Jacquet, Gibin Powathil, and Angélique Stéphanou. Modeling the role of hif in the regulation of metabolic key genes ldh and pdh: Emergence of warburg phenotype. *Computational and Systems Oncology*, 2(3):e1040, 2022. doi: 10.1002/cso2.1040. URL https://doi.org/10.1002/cso2.1040.

[35] Jui-Ling Yu, Hsiu-Chuan Wei, and Sophia R.-J. Jang. The role of cd4+ t cells in oncolytic virotherapy. *Mathematical Methods in the Applied Sciences*, 48(18):16652–16668, 2025. doi: https://doi.org/10.1002/mma.70115. URL https://onlinelibrary.wiley.com/doi/abs/10.1002/mma.70115.